PONTIFICIA UNIVERSIDAD CATOLICA DEL PERU
ESCUELA DE POSGRADO

Effect of thermal annealing treatments on the optical and electrical properties of aluminum-doped, amorphous, hydrogenated silicon carbide thin films.

Tesis para optar el grado de Magíster en Física

AUTOR

Luis Francisco Sánchez Sovero

ASESOR

Prof. Dr. Jorge Andrés Guerra Torres

JURADOS

Prof. Dr. Jan Amaru Palomino Töfflinger

Prof. Dr. Rolf Grieseler

Lima, Perú

2019

Abstract

In this work, a systematic study of the structural, optical and electrical properties of aluminum doped hydrogenated amorphous silicon carbide (Al-doped *a*-SiC:H) thin films grown by radio frequency magnetron sputtering is presented. The samples were grown using a high purity Al and SiC targets in a hydrogen-rich atmosphere and then were subjected to a rapid thermal annealing processes with temperatures of up to 600 °C. The film thickness ranged from 321 nm to 266 nm. The amorphous nature of the thin films was confirmed by X-ray diffraction measurements before and after the annealing treatments. Fourier transform infrared spectroscopy analysis revealed the different heteronuclear bonds present in the samples, whilst Raman spectroscopy showed the different homonuclear bonds present in the material. The evolution of the latter bonds with annealing temperature was assessed, showing a change in the structure of the thin film. Energy-dispersive X-Rays Spectroscopy confirmed the incorporation of aluminum in the amorphous silicon carbide matrix. UV-VIS Transmittance spectra revealed optical parameters such as Tauc energy bandgap, Iso-absorption energy bandgap and refractive index. Furthermore, the bandgap is also determined by means of a recently developed band-fluctuation model. In addition, electrical resistivity is determined by means of a four-probe Van Der Pauw method. Only the samples annealed at 600 °C exhibited contacts with an Ohmic behavior. The annealed films exhibited lower resistivities than the as-deposited ones, probably due to a thermal-induced reordering of the atoms. This reordering is shown in the variation of the Urbach energy which is related to an increase in the Si-C bond density, due to the dissociation of the hydrogen-related bonds.

Resumen

En este trabajo de tesis se presenta el estudio las propiedades estructurales y optoelectrónicas de carburo de silicio amorfo hidrogenado dopado con aluminio fabricado mediante pulverización catódica de radio frecuencia. Las muestras se fabricaron usando target de SiC y Al de alta pureza en atmosfera de hidrogeno. Luego las películas fueron calentadas hasta la temperatura de 600°C en un horno de rápido procesamiento térmico. La difracción de rayos X confirma la naturaleza amorfa de las películas. Los espectros de absorción infrarroja muestran los diferentes enlaces hetero-nucleares mientras que la espectroscopia Raman nos muestra los diferentes enlaces hononucleares presentes en la muestra. Se evaluó la evolución de los últimos enlaces con el tratamiento térmico, mostrando un cambio en la estructura del material. Espectroscopía de dispersión de energía de rayos X nos muestra la incorporación de aluminio en la matriz de carburo de silicio amorfo. Los espectros de transmitancia UV-VIS revelan parámetros ópticos tales como energía de Tauc, energía de Iso- absorción, energía de Tauc e índice de refracción. Además, el modelo de fluctuación de bandas desarrollado recientemente nos permite determinar los bordes de movilidad y energía de Urbach. Adicionalmente, el método de Van Der Pauw nos permite determinar el valor de la resistividad eléctrica de la muestra, solo a 600°C, donde se obtuvo un comportamiento óhmico mostrando baja resistividad eléctrica,

probablemente debido a un reordenamiento de los átomos inducidos térmicamente. Este reordenamiento estructural se muestra en la variación de la energía de Urbach que está asociada con el aumento de la densidad de enlaces Si-C, debido a la disociación de los enlaces relacionados con el hidrogeno.

Dedicated to my family, my parents and sister

for their support and concern at all times.

Also, to my girlfriend for her words of encouragement.

Acknowledgments

I would like to express my sincere gratitude to Prof. Dr Jorge Andres Guerra for his concern, guidance and understanding rendered throughout this work, especially for his invaluable support and patience in each moment. In addition, for their work motivation and the great friendship formed during all this time.

This work would have not been possible without the support of the Materials laboratory that is located in the physic section in which the samples were grown and studied. Furthermore, without the support of the Material Characterization Center (CAM), Center for productive Innovation and technology transfer (CITE), ubicated in Pontificia Universidad Catholica del Perú (PUCP), in which the optical and structural measurement were performed. In addition, the electrical and structural measurement were performed in Technische Universität Ilmenau (Germany), with the support of the Center for Micro-and Nanotechnologies (ZMN). This research was funded by the National Council for Science, Technology and Technological Innovation (CONCYTEC) of the Pontificia Universidad Catholica del Perú (PUCP).

This thesis was funded by the Concytec master scholarships contract number 233-2915-2 and was developed in the framework of the Concytec project with contract number 147-2017 FONDECYT led by Prof. Dr. Jorge Andres Guerra.

I am very grateful to Prof. Dr A. Palomino, Prof. Dr. Grieseler and Prof. Dr Andres Guerra for transmitting your knowledge and experiences in deposition issues, characterization of thin films, the use of experimental techniques used in this work as well as the foundations of photovoltaic. In addition, thank Mg. M. Mejia in a special way for the following: First, for the academic knowledge and wise advice transmitted. Second, for the unconditional support, trust and friendship have given in all this time. Also, mentioning that with order and discipline that she shows, she taught me that everything can be achieved. Finally, mention that her support was so important to complete this research work.

Further, I would like to thanks to Dr. Henry Romanus, M.Sc. Hauke-Lars Honig and Katrin Risch for providing access to their lab in order to perform the Van der Pauw technique, rapid thermal process, deposition of contacts on the sample and Infrared absorption by Fourier transform spectroscopy.

To all my colleagues of the doctorate in the MatER group, in special to Mg. Jorge Dulanto, Mg. Luis Conde, Mg. Paul Llontop, Mg. Roger Quispe and Mg. Carlos Torres for their collaboration. In addition, the group of partners of scholarships CONCYTEC, in special to Bs. Erick Serquen and Bs. Jose Luis Leon for being present when we need more and for the years we share in the master's degree.

Dedicatory 4

Acknowledgments 5

Index 6

1. Introduction 8

2. Fundamental theory 9

2.1 Wide bandgap semiconductors 9
2.2 silicon carbide 9
2.3 Optical properties of amorphous semiconductor 13
Atomic structure and electronic state density *13*
Fundamental absorption in amorphous semiconductor *15*
Tauc model *18*
Isoabsorption E_{04} energy *19*
Urbach energy *20*
Band-fluctuation model *20*
2.4 Electrical properties of amorphous semiconductor 22
Metal-semiconductor contact *22*
Van der Pauw method *29*
2.5 Structural properties of amorphous semiconductor 30

3. Experimental details 32

3.1 Deposition 32
3.2 characterization techniques 33
UV-VIS transmittance *33*
Infrared absorption by Fourier transform spectroscopy (FTIR) *35*
Raman spectroscopy *37*
Energy -*dispersion of X-Rays Spectroscopy (EDS)* *39*
dispersion of X-Rays (DRX) *42*
Mass spectroscopy (MS) *42*
van der Pauw technique *44*
3.3 Annealing treatments 45

4. Results and discussion 48

4.1 CHAMBER CONDITIONING **48**
4.2 STRUCTURAL ANALYSIS **54**
4.5 OPTICAL CHARACTERIZATION **65**
4.6 ELECTRICAL CHARACTERIZATION **72**

5. Conclusion **76**

6. References **79**

Introduction

Silicon carbide (SiC) is a wide band gap semiconductor (WBG) material with interesting physical, chemical and mechanical properties [1]. Due to these properties, SiC has been applied in solar cells, microelectronics, light emitting diodes, medical and photoelectrochemical applications. This material is of great interest due to the earth abundant composition, their simple and scalable thin film deposition technique, and their high stability in a corrosive environment [2][3]. One reason for this wide employment is that its band gap can be easily tuned from 1.8 eV to 3.1 eV by changing its stoichiometry, doping, incorporation of hydrogen and annealing treatment [4][5][6][7][8]. These tuning changes the light absorption property modifying other properties of *a*-SiC: H.

In the last decade, hydrogenated amorphous silicon carbide thin films (*a*-SiC: H) have been used as a photocathode material for water reduction in photoelectrochemical cells (PEC). Recently, an efficiency Solar-to-Hydrogen of 7.5% was reported [9]. These properties make SiC a promising material to be used as a photocathode in photoelectrochemical devices. Unfortunately, little is known about the aluminum doping and annealing treatment and its effect on the optical and electrical properties of (*a*-SiC: H). To know the properties of *a*-SiC: H(Al) film is important in order to asses' different applications, especially in photoelectroch emical devices, where the light absorption and electrical properties play a major role in the overall device efficiency and performance.

The goal of the current research is to obtain *a*-SiC: H(Al) thin films varying deposition conditions. One of the main aspects to produce high-quality *a*-SiC:H(Al) was the incorporation of heaters in the deposition chamber in order to reduce the humidity within in the chamber. Once low oxygen content films are obtained, the effect of an annealing treatment in a rapid thermal process furnace and doping on the structural, electrical and optical properties is of major importance and systematically studied in this thesis.

Fundamental theory

2.1 Wide-bandgap semiconductors

Wide bandgap (WBG) semiconductors materials which have a relatively large band gap compared to typical semiconductor materials. Those materials are employed in optoelectronic and alternative energy devices such as light emitting diodes, white light illumination, high-frequency /high-power diodes and fuel cell devices [10]. The three main types of wide bandgap semiconductors are group III nitrides, group II oxides, group II chalcogenides, IV-IV compounds and diamond. The bandgap versus lattice constant of the principal WBG semiconductors at room temperature is shown in Figure 2.1.

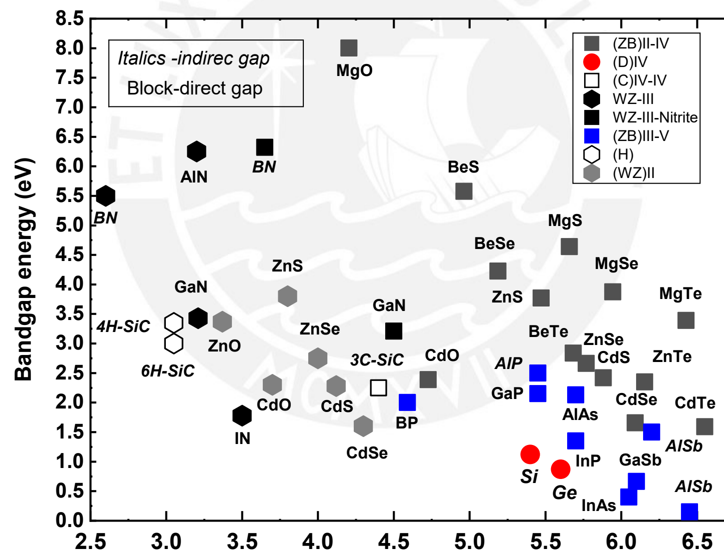

Figure 2.1 Relationship between forbidden energy gap and lattice constant of WBG [10].

2.2 Silicon carbide

Silicon carbide (SiC) is a binary WBG semiconductor, which can occur in more than 250 crystalline forms called polytypes. The most common ones are 3C, 4H, 6H and 15R. SiC polytypes consist of silicon atoms bonded with four carbon atoms in a tetrahedral arrangement as shown in Figure 2.2.1. In addition, they are differentiated by the stacking sequence of each tetrahedrally bonded Si-C bilayer and thus by the band gap energy and electronic properties as

well [11]. The advantages of silicon carbide over the other WBG semiconductors are physical, chemical and mechanical properties such as high thermal conductivity, mechanical hardness, high melting point, chemical resistance, high refractive index and wide (tunable) band gap [1]. Finally, in Table 2.2.1 shows some properties of mean polytypes of silicon carbide compared to silicon.

The main motivations for using hydrogenated amorphous silicon carbide (*a*-SiC:H) films compared to other semiconductors such as silicon are is its high chemical stability, tunable wide band gap energy between 1.8 eV to 3.1 eV [1][6][12]. *a*-SiC:H has been prepared by various methods, such as the chemical vapor deposition (CVD) [13], high-energy ion irradiation [14], physical vapor deposition (PVD) [15] and R.F sputtering [6][16][17]. The structural and optoelectronic properties of these films depend on the deposition methods and preparation conditions. These conditions can be the type of the sputtering gases, the chamber pressure, deposition time and substrate temperature.

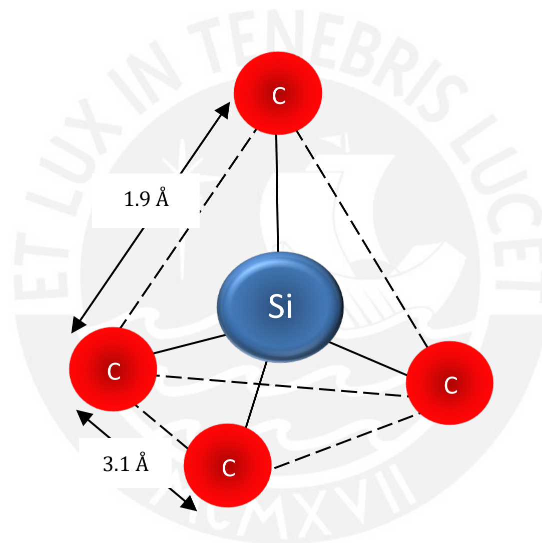

Figure 2.2.1 Schematic diagram of tetrahedral bond of silicon carbide [10].

Table 2.2.1 Physical properties of polytypes of silicon carbide as well as silicon for comparison at 300 *K* [18][19]

	6H SiC	**4H SiC**	**3C SiC**	**Si**
Energy gap *(eV)*	3.02	3.26	2.40	1.12
Thermal conductivity *(W/cm)*	4.9	3.7	3.2	1.5
Dielectric constant	10.3	9.7	9.7	11.8
Refractive index	2.65	2.55	2.69	2.4
Transition	indirect	indirect	indirect	indirect

a-SiC: H has the potential to be used in a number of applications such as optoelectronic, renewable energy, biomedical among others. For instance, *a*-SiC:H films can be used as an absorber layer in a semi-transparent solar cell for its flexibility in controlling its optical parameters [20], a biomedical microdevice for its potential as a structural and packing material [21], a potential semiconductor for quantum computing [22], a hermetic encapsulate device for the integrated silicon-based neural interface devices [23] and in particular, *a*-SiC:H has received a growing interest as photo-electrode material for photoelectrochemical (PEC) water splitting which is becoming a feasible and important method for solar energy conversion in the form of hydrogen fuels [3].

Thus, *a*-SiC:H is used as photo-electrode due to the easy production method and its relatively high resistance to corrosion when in contact with the electrolyte, which is important in order to prolong the lifetime of the device. Moreover, it has a tunable band gap energy as is shown in Figure 2.2.2(b), which allows the integration of multi-junction photovoltaic (PV) with smaller band gaps (*i.e*, 1.12 eV - 1.80 eV) to form tandem light absorbers for maximum spectral utilization, which allows obtaining a high solar to hydrogen (STH) efficiency. In this context, recently an efficiency of 7.9 % has been reported [9]. Further, p-type *a*-SiC:H layers has been reported an enhanced conversion efficiency [8][24].

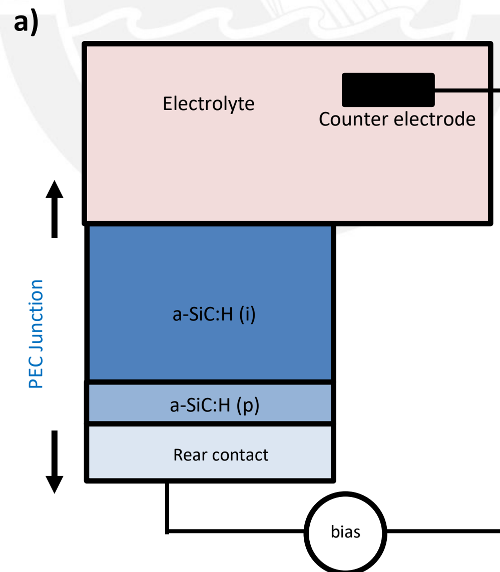

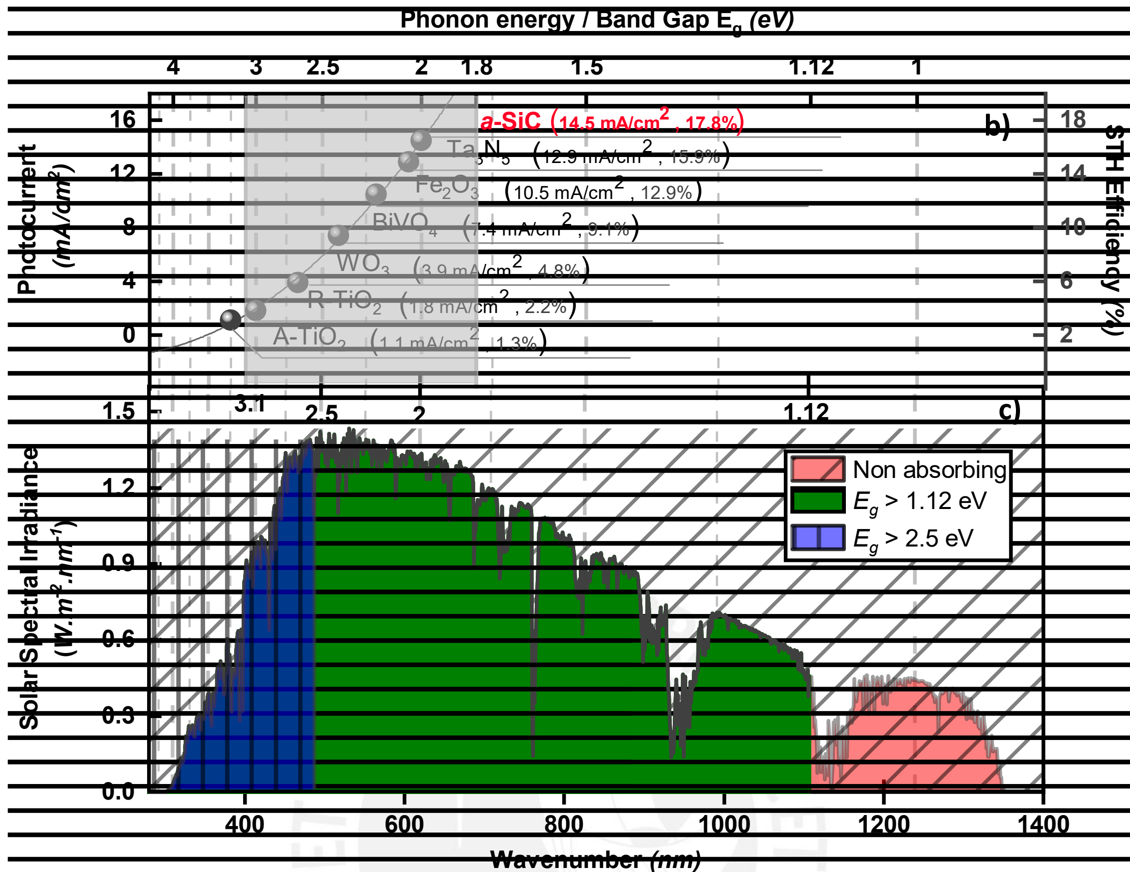

Figure 2.2.2 Schematic illustration of a PEC configuration. Scheme taken from [9] (a). Maximum current and STH efficiency available as a function of bandgap of materials enabled to be used as photo-electrode. The grey box is indicated the values of energy that can be take *a*-SiC:H (b). Solar spectral irradiance against wavenumber in order to show the absorption spectral to different bandgap as silicon (1.12 eV) and silicon carbide (2.5 eV) (c).

2.3 Optical properties of amorphous semiconductors

Prior to discuss the absorption coefficient and its implication on the bandgap. It is appropriate to understand the differences between crystalline and amorphous semiconductors materials and their electronic density of states.

Atomic structure and electronic state density

The amorphous semiconductor is different from the crystalline material mainly due to the disorder of the atomic structure. A crystalline material presents a periodic array of atoms throughout the solid, thus shows a long-range order (see Figure 2.3.1). Whereas, the amorphous counterparts presents only a short-range order and long-range disorder in which each atom has a

specific number of bonds (coordination defect), different bonds angles, different bond length to its immediate neighbors [25].

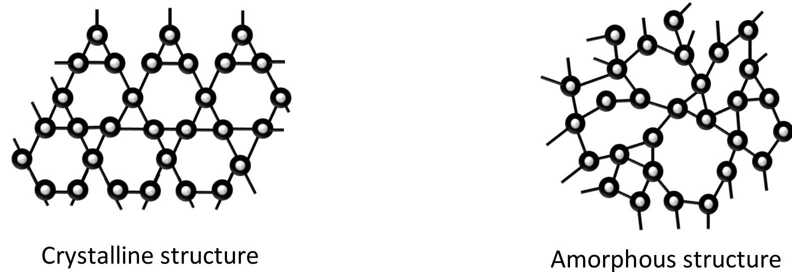

Figure 2.3.1 An illustration contrasting the crystalline and amorphous structure in two dimensions.

The origin of the energy band gap in amorphous semiconductors does not result from the material's structural order but from the chemistry of their bonds. The band structure is formed due to the covalent bonding of atoms, which is can be described by the linear combination atomic orbital (LCAO) method. The obtained result of this bond of an isolated atom is divided into two energy levels when two atoms are brought close together and interact. The lowest energy state is known as bonding orbital and its lower than the energy of the state of isolated individual atoms. The higher energy is called anti-bonding orbital, as is shown in Figure 2.3.2. This energy separation of the bonding and anti-bonding states depends on the distance R between atoms. The energy band gap reduced when the distance increases [26]. This behavior can be extended for the interaction of many atoms, which allows the formation of quasi-continuum states as demonstrated by Weaire and Thorpe (1971) through the *tight binding approach*, where they showed that a discontinuity in the electronic density of states is founded separating the valence and conduction bands and hence leading to the formation of a bandgap [26]. These quasi-continuum states are called as valence and conduction extended states in amorphous material case.

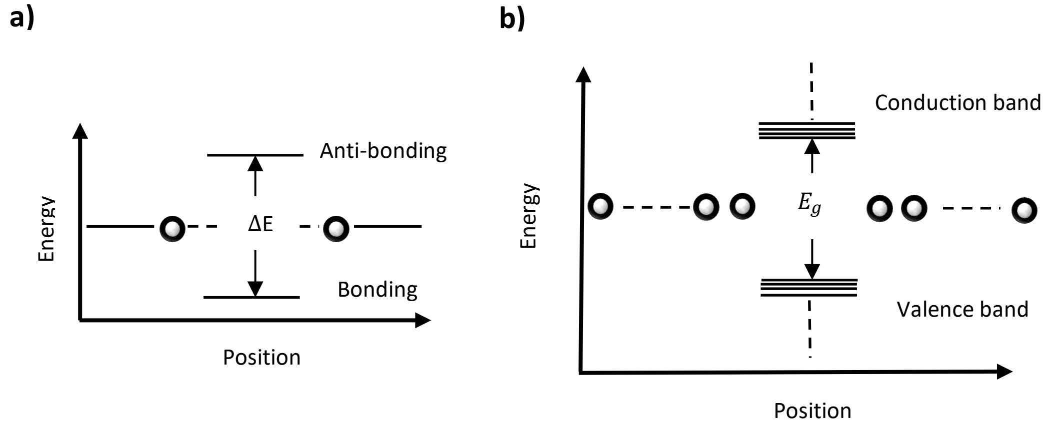

Figure 2.3.2 Illustration of the bonding and anti-bonding of two atoms. When the bond is made two energy levels are formed (a). Representation of quasi-continuum states of the interaction of many atoms for forming of a bandgap (E_g) (b).

Thus, the formation of energy bands is a result of bonding and antibonding orbitals states. The density of states $g(E)$ for valence and conduction band in crystalline semiconductor is described by the quasifree electron approximation (see equation 2.3.1). Here, $\hbar$ is Planck constant, $m^*_{e/h}$ is the electron and hole effective mass, $E_c(0)$ and $E_v(0)$ are arbitrary constants. The formation of the density of states can be seen Figure 2.3.3.

$$g_c(E_c) = \sqrt{2}\frac{m_e^{*\,3/2}}{\pi^2\hbar^3}\left(E_c - E_c(0)\right)^{1/2}$$
$$g_v(E_v) = \sqrt{2}\frac{m_h^{*\,3/2}}{\pi^2\hbar^3}(E_v(0) - E_v)^{1/2} \qquad (2.3.1)$$

Where bandgap is the difference between bottom of conduction band and top of valence band. Amorphous semiconductors present extended states due to the influence of the short-range order, equal like crystalline material. In addition, Figure 2.3.3 can see important changes in bandgap. The presence of deviations of the bond length and angles arising from long range structural disorder in amorphous material is resulting in localized tail states that can overlap the extended states. Additionally, other localized states are present near the middle of gap called dangling bonds. These states arise from defects in an ideal network, such as coordination defects, which have three possible charge states: neutral, positive and negative charge. Energies denoted by E_v and E_c are borders between extended and localized states and corresponding to the mobility edges. The distance between both mobility edges is known as mobility gap, which is similar to the band gap for crystalline material [25][26].

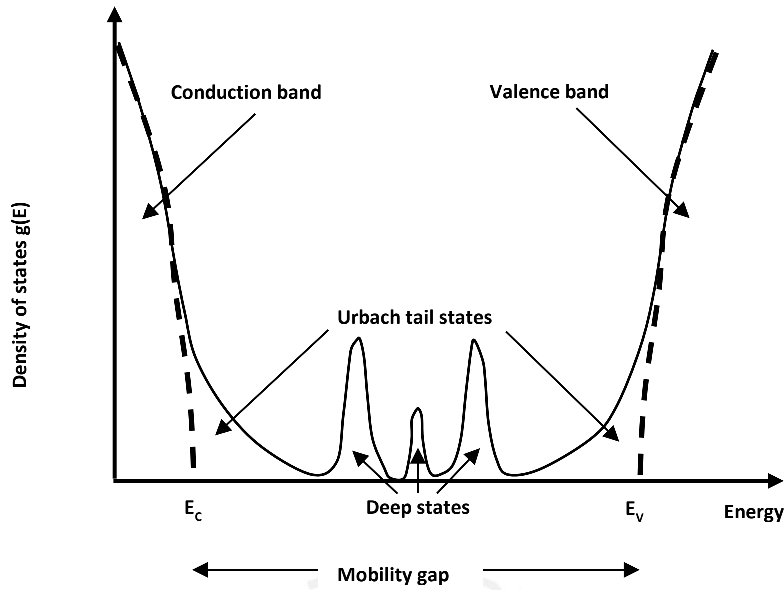

Figure 2.3.3 Schematic density of states distribution for an amorphous semiconductor showing the bands, the band tails, and the defects states in the band gap. The dashed curves are the equivalent density of states in a crystal.

Fundamental absorption in amorphous semiconductors

The absorption coefficient α gives information about electronic states and this later contains information of the bandgap energy, tail states and the degree of disorder. Figure 2.3.4 shows the representative shape of the absorption coefficient in the UV-VIS-NIR spectral region for an amorphous material. Three principal zones can be identified: strong absorption edge arises to the fundamental absorption or Tauc region and corresponding to the band-to-band electronic transitions, the medium absorption region shows an exponential behaviour, which is known as Urbach region due to tail states corresponding to band to tail transitions and finally, a low absorption region corresponding to transitions involving defect states deep within the forbidden gap.

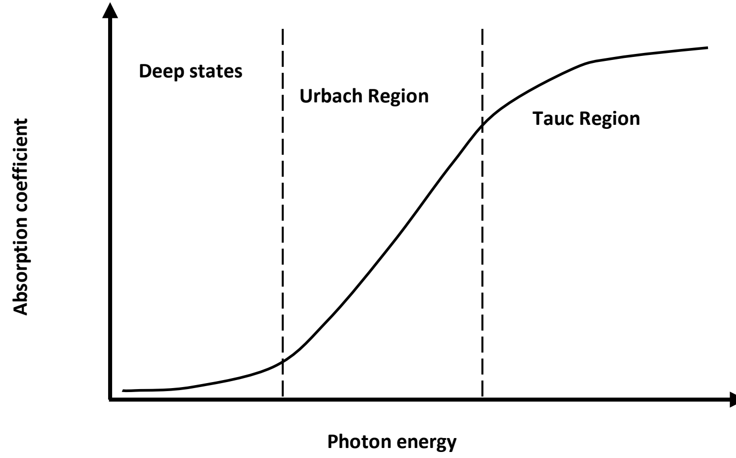

Figure 2.3.4 Schematic plot of the representative shape of the absorption coefficient in logarithmic scale of amorphous semiconductors in the UV-VIS -NIR spectral region.

All these electronic transitions are associated to the interaction of material with electromagnetic radiation (UV-VIS-NIR frequency), where the absorption process is studied using perturbation theory. In this sense, the power per unit volume absorbed by a material W_M is connected to the electronic transition rate probability per unit volume R_{cv} by $W_M = R_{cv}\hbar\omega$ .This is equal the energy density rate per unit volume delivered by the electromagnetic wave $W_R = -d\langle U\rangle/dt$, which is related to the absorption coefficient. Thus, the absorption coefficient α is related to the electronic transition rate per unit volume due to optical excitation energy between the extended valence states and conduction states by equation 2.3.2 where *n* is the index of refraction, *c* is the speed of light, ϵ_0 the electric permittivity constant in vacuum and $|\mathbf{E}|$ the electric field amplitude [27].

$$\alpha \frac{nc\,\epsilon_0}{2}|\mathbf{E}|^2 = R_{cv}\hbar\omega \qquad (2.3.2)$$

Now, the transition probability rate R_{cv} can be written using the Fermi's Golden Rule, which indicates the transition probability from the valence and conduction band by photon absorption per unit time per unit volume due to perturbation of the photon energy incident on the material $H_{eR} = e\,\boldsymbol{p}\cdot\boldsymbol{A}/m_e$, is present in the equation 2.3.3. Here, $E_{c/v}$ and $\boldsymbol{k}_{\boldsymbol{c}/\boldsymbol{v}}$ are the electron energy and the electron wave vector at the conduction and valence states respectively. $|M_{cv}|$ is the transition matrix element in the dipole approximation given by $|M_{cv}|e/m_e = \langle c|H_{eR}|v\rangle$ [27].

$$R_{cv} = \frac{2\pi}{\hbar}\left(\frac{\mathbf{E}\, e}{2m_e\omega}\right)^2 \sum_{k_c, k_v} |M_{cv}|^2 \delta(E_c - E_v - \hbar\omega)\delta_{k_c, k_v} \qquad (2.3.3)$$

Then, from the equation 2.3.2 and 2.3.3, the absorption coefficient can be expressed by equation 2.3.4. Where δ is related to the momentum and energy conservation. For the direct absorption process $\boldsymbol{k_c} = \boldsymbol{k_v}$, which obeys conservation of momentum. On the other hand, in indirect absorption exist different wave vector $\boldsymbol{k_c} = \boldsymbol{k_v} \pm \boldsymbol{k_\phi}$ as can be seen Figure 2.3.5.

$$\alpha = \frac{\hbar}{4\pi\epsilon_0 nc}\left(\frac{2\pi e}{m_e}\right)^2 \frac{1}{\hbar\omega} \sum_{k_c, k_v} |M_{cv}|^2 \delta(E_c - E_v - \hbar\omega)\delta_{k_c, k_v} \qquad (2.3.4)$$

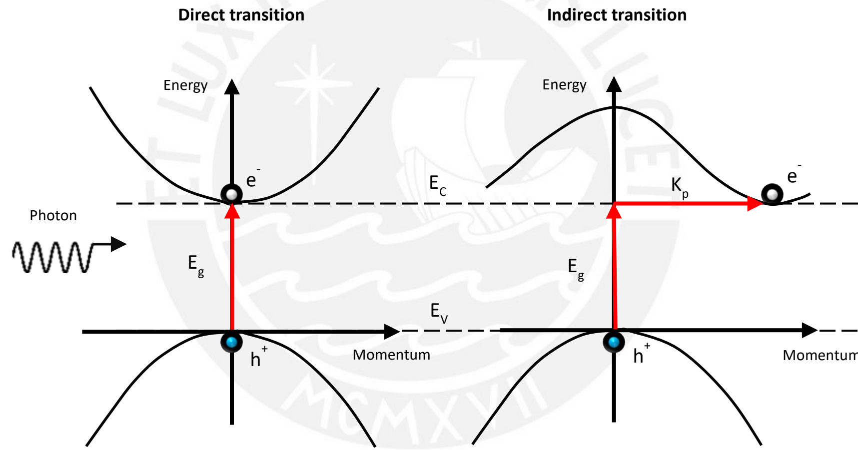

Figure 2.3.5 Energy-momentum diagram of direct and indirect transition, the diagram left side shows the excitation of an electron from the valence to conduction band after absorber a photon (diagram left side). Whilst the other diagram illustrates the absorption of a photon assisted by phonon to reach the excitation.

For direct and indirect transition, the transition matrix elements $|M_{cv}|^2$ is assumed that varies slowly with the photon energy. Furthermore, the summation over the vector $\boldsymbol{k}$ can be collocated as a summation over the energy due to energy bands dispersion relation. This can be calculated by the density of states [26] as is shown in equation 2.3.5. Then, from equation 2.3.5 in equation 2.3.4, the absorption coefficient direct and indirect for amorphous material is expressed in the equation 2.3.6. Here $\alpha_0 = \frac{\hbar}{4\pi\epsilon_0 nc}\left(\frac{2\pi e}{m_e}\right)^2$.

$$\sum_{k_v} \sum_{k_c} \rightarrow \int g(E)dE \tag{2.3.5}$$

$$\alpha_{direct} = \frac{\alpha_0}{\hbar\omega} \int_{E_{cv}(0)}^{\hbar\omega} g_{cv}(E_{cv})\delta(E_{cv} - \hbar\omega)dE_{cv}$$
$$\alpha_{indirect} = \frac{\alpha_0}{\hbar\omega} \int \int g_c(E_c)g_v(E_v)\delta\big(E_c - E_v - \hbar\omega \pm E_\phi\big)dE_v dE_c \tag{2.3.6}$$

Tauc model

Using, the Tauc model it is possible to extract the optical bandgap energy, as this model has been widely applied to amorphous materials for various authors [6][28][29][30]. Tauc model proposes to take the form of free electron approximation seen in equation 2.3.1. Solving the integral in equation 2.3.6 together with the equation 2.3.1. The absorption coefficient can be written as follows [30]:

$$\alpha_{Tauc} = M_{Tauc} \frac{(\hbar\omega - E_{Tauc})^2}{\hbar\omega} \tag{2.3.7}$$

Here, M_{Tauc} includes all constants, $\hbar\omega$ is the energy of incident photons. To extract the value of optical bandgap $(\alpha h\nu)^{1/2}$ versus $(h\nu)$ should be plotted and a linear fit on the fundamental absorption region should be performed. The intercept of the linear fit with the energy axis is the value of the Tauc-energy bandgap, as shown in Figure 2.3.7 On the other hand, as it was mentioned before in the prior section, the band tails play a crucial role on the optical property and in fact they show a strong influence in the optical bandgap. Therefore, the Tauc-gap is used as a representative value of the “correct” gap.

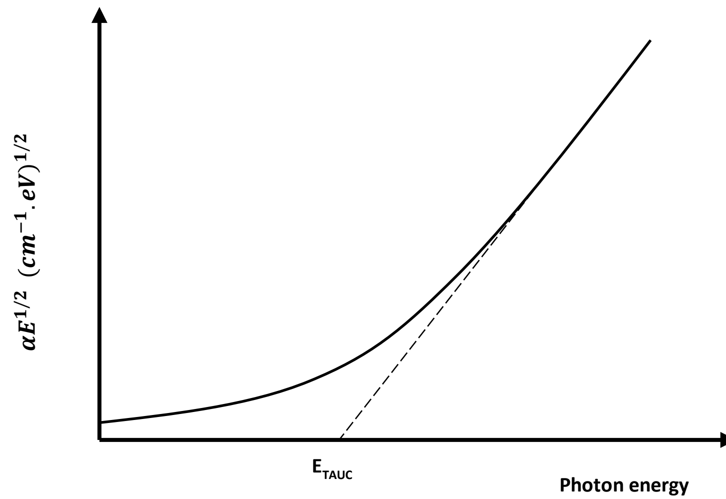

Figure 2.3.7 Tauc-plot graphic showing a linear fit the high energy region.

Isoabsorption E_{04} Energy

The value of E_{04} is another possibility used by some authors[29][31] in order to compare bandgap energy values. The E_{04} value is determined by plotting the absorption in the logarithmic scale against photon energy plot. The isoabsorption energy value is assigned where is the absorption coefficient has a value of 10^4 cm^{-1}, see Figure 2.3.8.

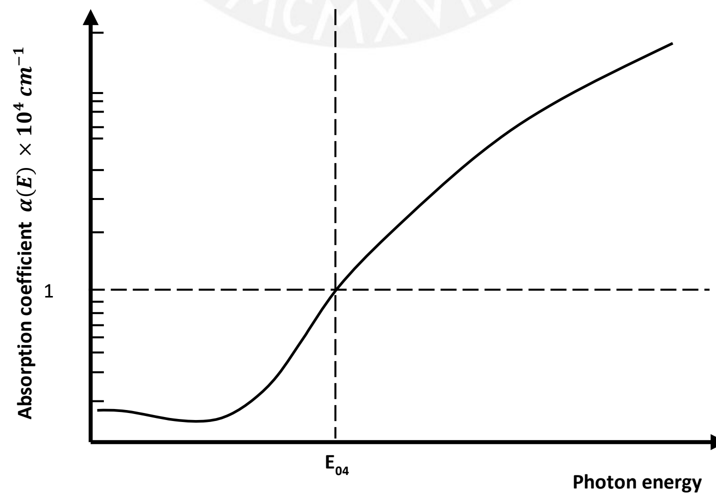

Figure 2.3.8 Absorption coefficient in logarithmic scale versus photon energy graphic.

Urbach energy

As mentioned in the previous section, the origin of band-tail states in amorphous semiconductors is mainly due to structural disorder, defects and even temperature effects.

Below the fundamental region, Urbach region, typically the band-tails observed in the absorption coefficient can be given by an exponential behavior. Here, the transitions of tail-states to extended band structures is evidenced (See equation 2.3.5.1) [6][28].

$$\alpha(E) = \alpha_F \exp\left(\frac{E - E_F}{E_u}\right) \tag{2.3.8}$$

As can be seen in Figure 2.3.2.1, in logarithm scale, the equation 2.3.5 will be written by written as shown in equation 2.3.9.

$$\log(\alpha(E)) = log(\alpha_F) + \left(\frac{E - E_F}{E_u}\right) \tag{2.3.9}$$

Here, α_F and E_F are constants and E_u is Urbach energy, which can be extracted of the inverse of the slope of a linear fit in Urbach zone. This value ranges regularly from ~10 meV to ~200 meV. Thus, the Urbach energy is an indirect measure of the degree of disorder and thermal vibration in the amorphous material [32]. Another possibility to measure the degree of disorder is to determine the average bond distance and angle variation, which can be calculated from the width at half maximum of vibration spectral using infrared absorption spectrum or Raman spectrum.

Band-fluctuation model

This model is developed to describe the sub-bandgap exponential band tail and the fundamental absorption observed in the optical absorption of amorphous semiconductors. According to Guerra *et al*. [33], considering that the topologic disorder and thermal vibration in amorphous material have the same behaviour, provides the chance to model both effects by only thermal vibration, due to that at high temperature the amorphous material can be considered as ordered, in which the molecules are frozen in time. This is known as frozen phonon model.

In order to calculate the absorption coefficient in amorphous material, the frozen phonon model is taken account and is necessary determine the average electronic transition rate R_{cv} between the conduction and valence band. Extending the one-electron approximation considering: *i*) the electronic occupation degree in the valence band using $g_c \rightarrow g_c(E_c) \times \left(1 - f(E_c)\right)$ *ii*) the available states in the conduction band using $D_v \rightarrow D_v(E_v) \times f(E_v)$ and *iii*) the stimulated relaxation process in the Fermi's Golden rule absorption coefficient can be achieved as shown equation 2.3.10. The equation 2.3.10 is known as the Kubo-Greenwood formula, which is used to describe the temperature dependence of the electrical properties of a semiconductor [28][33]. Moseley *et al.* [34] following the approach of Kubo-Greenwood defined the average electronic

transition rate versus temperature as is shown in equation 2.3.11. Here $f(E)$ is the Fermi distribution.

$$R_{cv}(\hbar\omega) = \frac{2\pi}{\hbar}\left(\frac{\tilde{E}e}{2m_e\omega}\right)^2 \sum_{k_c,k_v} |M_{cv}|^2 \{f(E_v) - f(E_c)\}\delta(E_c - E_v - \hbar\omega) \qquad (2.3.10)$$

$$\langle R_{cv}\rangle(T) = \int R_{cv}(E)|_{T=0} \left\{\frac{-d(f(E))}{dE}\right\} dE \qquad (2.3.11)$$

Furthermore, O'Leary proposed treating the JDOS (joint density of states) as a local JDOS over the distribution of conduction and valence bands with a Gaussian distribution to take into account the thermal fluctuations [35].

$$\langle J_{cv}\rangle(E_{cv}) = \int_{-\infty}^{\infty} \widehat{W}(\epsilon - E_{cv}) g_{cv}(\epsilon) d\epsilon \qquad (2.3.12)$$

Here $\widehat{W}$ is the weight function, that should produce the tail states below the fundamental absorption, $E_{cv} = E_c - E_v$, where E_v and $E_c$representing the valence and conduction band energy, respectively and J_{cv} is joint density of states.

Now, starting from the equation 2.3.11, Guerra *et al* used $-f'(\hbar\omega)$ as weighting function which is similar to a Gaussian type distribution and $\lim_{T\to 0} -f'(\hbar\omega, T) = \delta(\hbar\omega)$, called Dirac Delta function of the traditional Tauc calculation. Thus, the average of the Join Density of States was proposed as shown in equation 2.3.13.

$$\langle J_{cv}\rangle(E_{cv}) = \int_{-\infty}^{\infty} -f'(\epsilon - E_{cv}) g_{cv}(\epsilon) d\epsilon \qquad (2.3.13)$$

Then, introducing the average JDOS into the Fermi's Golden Rule (see equation 2.3.3) and considering the relaxation of the momentum conservation the average electron transition rate can be written as shown in the equation 2.3.14. This equation is equal to the electronic transition rate at zero Kelvin for direct transition except the Dirac Delta function term, which is changed by a Fermi distribution derivate.

$$\langle R_{cv}\rangle(\hbar\omega, T) = \frac{2\pi}{\hbar}\left(\frac{\tilde{E}e}{2m_e\omega}\right)^2 \int |M_{cv}|^2 D_{cv}(E_{cv})\{-f'(E_{cv} - \hbar\omega)\} dE_{cv} \qquad (2.3.14)$$

Finally, by integrating equation 2.3.14, it can be written in the form more compact from using $\mathrm{Li}_2(x)$, which is the Dilogarithm function of x .

$$\alpha(\hbar\omega) = -\frac{\pi}{4}\frac{\alpha_0}{\beta^2\hbar\omega}\mathrm{Li}_2\left(-e^{\beta(\hbar\omega-E_0)}\right) \tag{2.3.15}$$

Here $\beta = 1/(k_B T)$ is the definition of the Urbach slope and E_0 is defined as the energy difference between the mobility edges. This model includes the distributions of band-to-band and tail states transitions. The asymptotic analysis of equation 2.3.15 leads to identical Urbach and Tauc equations. Theses equation are called extended Tauc and Urbach by Guerra [33].

$$\alpha(\hbar\omega) = \frac{\pi}{8}\frac{\alpha_0}{\hbar\omega}\begin{cases} \dfrac{2}{\beta^2}e^{\beta(\hbar\omega-E_0)} & , \quad \hbar\omega \ll E_0 \\ (\hbar\omega - E_0)^2 + \dfrac{\pi}{\beta^2} & , \quad \hbar\omega \gg E_0 \end{cases} \tag{2.3.16}$$

Fluctuation bands approach models allows to calculate both the fundamental absorption region and the Urbach tail region of the optical absorption.

2.4 Electrical properties of amorphous semiconductors

Prior to discuss about the electrical conductivity of amorphous semiconductors, it is convenient to understand the basic foundations of the metal-semiconductors junction and the technique used to determine the electrical conductivity of amorphous thin films semiconductors.

Metal-semiconductor contacts

The study of the semiconductor-metal junction is of great relevance as most devices based on semiconductor materials have a metal-semiconductor junction.

Furthermore, in particular for applications in photoelectrochemical devices, there are two possible situations, depending on the material properties, that can occur at the junction:

a) Ohmic contact, which has a low contact resistance junction providing conduction in both directions between metal and semiconductor. Ideally, the current through this type of contact is a linear function of an applied voltage.
b) Schottky contact, which presents a rectifying behavior, in one way, similar to p-n-semiconductor junction [36].

In the following, the main characteristics and properties of this semiconductor-metal junction are presented. In order to study the behavior of the semiconductor-metal junction, first, three parameters should be defined.

a) The work function of the metal Φ_M indicates the energy necessary to remove an electron from Fermi level of material to vacuum level.
b) The work function of semiconductor Φ_{SC} depends on the doping concentration as the Fermi level depends on doping type and concentration.
c) Electron affinity χ_{SC} is the difference between the conduction band of the semiconductor and the vacuum level.

Schottky contacts

To obtain an ideal Schottky or rectifying contact, the following must be fulfilled in the case of a metal and n-type-semiconductor ($\Phi_M > \Phi_{SC}$), and for the opposite case ($\Phi_{SC} > \Phi_M$).

Without any contact, the Fermi level of the semiconductor is above the metal fermi level. For the Fermi level to become constant throughout the system (thermal equilibrium), the electrons from the semiconductor flow into the lower energy states in the metal. The positively charged donor atoms remain in the semiconductor, creating a space charge region that it is known as depletion zone. On the other hands, in order to maintain the neutrality of the junction, a negative charge appears at surface of the metal. This causes an electrical field from the semiconductor to the metal. This electrical field produces a potential variation in the semiconductor that results in the bending of the energy bands.

Figure 2.4.1 shows an ideal energy-band diagram in contact between metal and n-type-semiconductor. The parameter Φ_{Bn} is the ideal barrier height of the semiconductor contact, the electrons in the metal feel the potential barrier and try to move into the semiconductor. This barrier is known as the *Schottky barrier* and is given by equation 2.4.1. Where the Schottky barrier is the difference between Fermi level and the conduction band in the interface.

$$\Phi_{Bn} = (\Phi_m - \chi_{SC}) \quad (2.4.1)$$

Furthermore, V_{bi} is the built-in potential barrier. The electrons feel this barrier in the conduction band trying to move into the metal. The built-in potential barrier is given by equation 2.4.2. Which makes that V_{bi} depends on semiconductor doping.

$$V_{bi} = (\Phi_{Bo} - qV_n) \tag{2.4.2}$$

On the other hand, if the boundary conditions are considered in the Poisson equation, a charge density volume and a uniform doping is possible to obtain the space charge region width W as shown equation 2.4.3. Here N_D is doping concentrations of semiconductor, K is Boltzmann constant, T is the temperature in Kelvin and $\in_s$ is the dielectric permittivity of semiconductor [36][37][38].

$$W = \sqrt{\frac{2 \in_s (V_{bi} - KT/q)}{qN_D}} \tag{2.4.3}$$

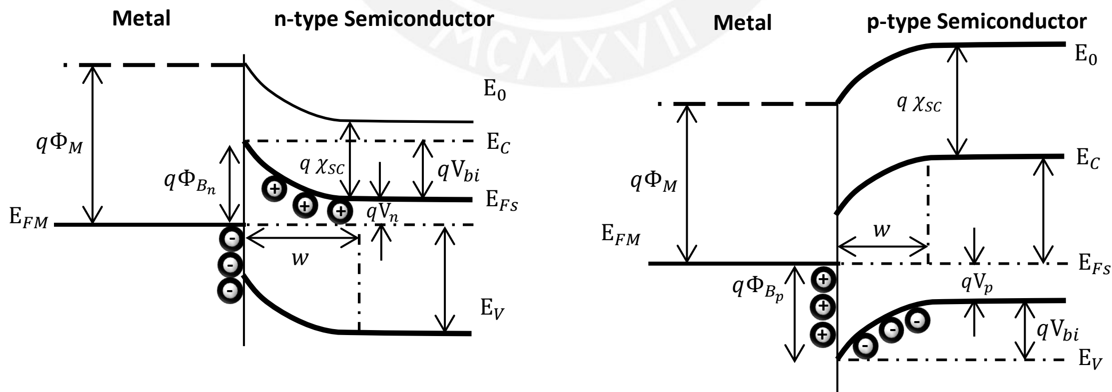

Figure 2.4.1. Ideal energy-band diagram of a metal in contact with a n-type semiconductor moderately doped ($\Phi_M > \Phi_{SC}$) and p-type ($\Phi_{SC} > \Phi_M$). Here E_V is valence band energy level, E_c is conduction band energy level and E_{FS} is Fermi level.

In this situation, the net current through this contact is nonlinear, as the current flow preferably in one way (from semiconductor to metal) but not at the opposite way. It is known as rectifying the contact.

Finally, for case metal and p-type semiconductor junction the previous considerations are valid, except that the majority charge carrier are holes.

Ohmic contacts

For obtaining an ideal Ohmic contact, the following must be fulfilled in case of metal and n-type-semiconductor $\Phi_M < \Phi_{SC}$, and for the opposite case $\Phi_M > \Phi_{SC}$. An ohmic contact is independent the doped semiconductor properties. The Schottky barrier value is smaller than qV_n or even zero. Figure 2.4.2 shows an ideal energy-band diagram after contact between metal and n-type semiconductor. The Fermi level become constant throughout the system (thermal equilibrium) when the electrons from the semiconductor flow into the lower energy states in the metal. To reach thermal equilibrium between the metal and the n-type semiconductor, the electrons flow from metal into the semiconductor creating an electric field within the semiconductor as a consequence of accumulative charge in the interface which produces energy band bending. For the case of metal - p-type semiconductor junction occurs at the inverse situation.

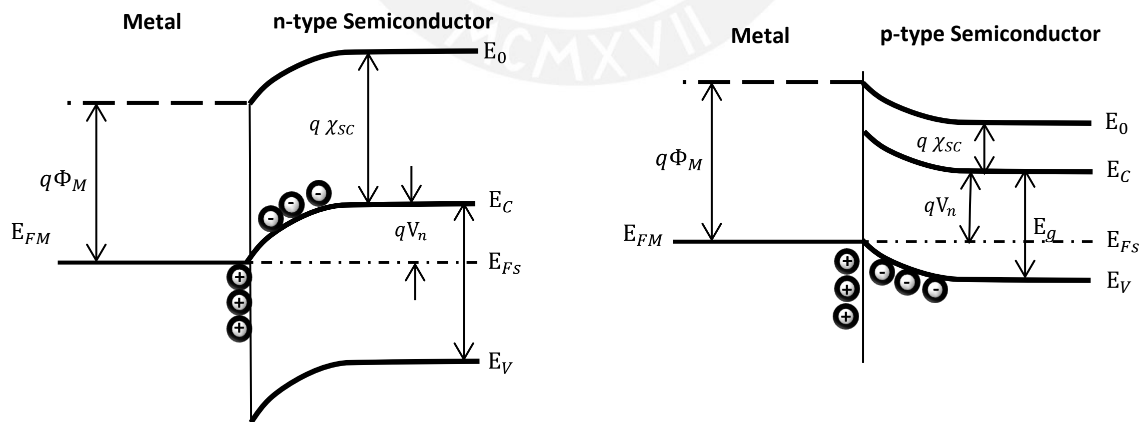

Figure 2.4.2. Ideal energy-band diagram after contact for a metal-n-type semiconductor junction for $\Phi_M < \Phi_{SC}$, the right-side metal p-type semiconductor junction for $\Phi_M > \Phi_{SC}$.

The ohmic contact quality is evaluated by its contact resistance R_c, that is defined by equation 2.4.4 for small concentration values of N_D. The thermionic emission process is dominant in this case.

$$R_c = \frac{KT}{qA^*T^2} e^{\frac{q\Phi_{Bn}}{KT}} \tag{2.4.4}$$

For high doping concentration values of N_D, the width of the potential barrier is very small. Here the tunneling process is dominant. Thus, the specific resistance is founded by equation 2.4.5 [36].

$$R_c \sim e^{\frac{+2\sqrt{m^* \epsilon_s}}{\hbar}\left(\frac{\Phi_{Bn}}{\sqrt{N_D}}\right)} \tag{2.4.5}$$

Schottky barrier under bias

The Schottky barrier formation under bias is analyzed. For the ideal case, metal the effect caused by interface states that exist in the interface metal-semiconductor and the distortion of the potential barrier due to the electric field image-force are not considered. Information about these effects can be found in the following references [36][39].

This junction can be undergone under reverse and forward bias. Both biases change the potential barrier and the space charge region width as is shown in Figure 2.4.3 for metal-n-type semiconductor junction case.

If a positive voltage V_F is applied to the metal with respect to the semiconductor (forward bias), the semiconductor-to-metal barrier height (qV_{bi}) and depletion zone are reduced while that $q\phi_n$ remains constant in this idealized case. In this sense, electrons can flow easier from the semiconductor into the metal as shown in Figure 2.4.1.3 (a). If we apply positive voltage V_R to the semiconductor with respect to the metal (Reserve bias), the semiconductor-to-metal barrier height and depletion zone are increased and the flow of electrons from semiconductor to metal is reduced.

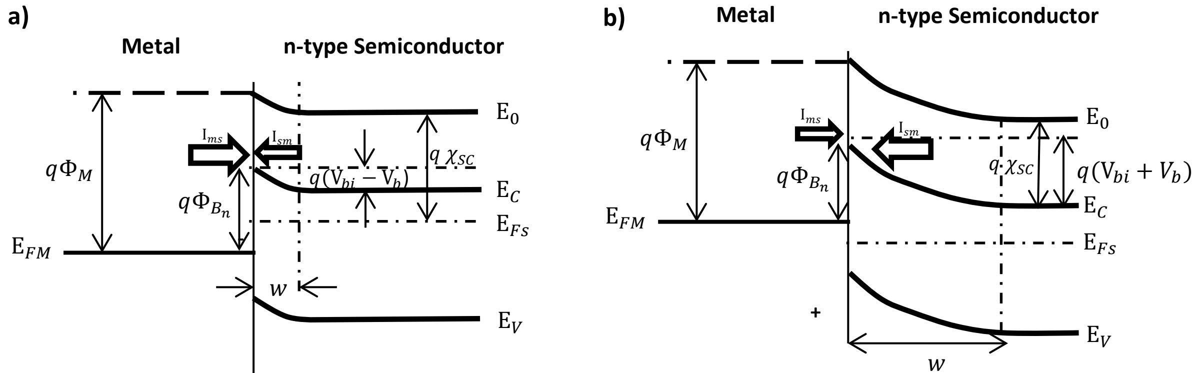

Figure 2.4.3. Ideal energy-band diagram for a metal-n-type semiconductor contact. (a) meta-semiconductor under Forward bias V_F (b) metal-semiconductor under Reserve bias V_R. I_{SM} is the flow of electrons from semiconductor to metal and I_{MS} is the flow of the electrons from metal into the semiconductor.

Conduction mechanism of Schottky contact

The basic concepts of the metal-semiconductor junction have been presented. It has been shown the different transport mechanisms in the Schottky contact. The current transport in a metal-semiconductor junction is due mainly to the majority carrier. The main transport mechanisms are:

a) TE: Thermionic emission
b) TFE: Thermionic field emission or tunneling effect
c) FE: Field emission

a) Thermionic emission current

In forward bias, a metal on a lightly doped semiconductor, this transport mechanism is dominant where the electrons must overcome the potential barrier. The current is controlled by the number of electrons with excess energy higher than the barrier to go towards the metal surface. This is expressed by equation 2.4.6. Here, A is the transversal section area from the metal-semiconductor interface, A^* is the Richardson constant and $\Delta\phi$ is the effective to bias through to the interface and T is the temperature.

$$I \sim AA^*T^2 e^{-\frac{q\Phi_{Bn}}{KT}}(e^{-\frac{q\Delta\phi}{KT}} - 1) \quad (2.4.6)$$

b) Thermionic field emission and field emission current

Tunneling is a quantum-mechanical phenomenon. In this context an electron can be represented by a wavefunction. The wavefunction does not terminate abruptly on the potential barrier and it can penetrate into the barrier. So, the quantum probability that this phenomenon occurs is not zero. For high doping semiconductor, this transport mechanism is dominant. The tunneling current can be represented by equation 2.4.7, where I_{tno} is the saturation current by tunneling and E_{00} is a parameter related to the properties of the semiconductor material.

$$I \sim I_{tno}(e^{\frac{qBn}{E_{00}}} - 1)$$
$$E_{00} = \frac{q\hbar}{2}\sqrt{\frac{N_D}{m^* \epsilon_s}} \qquad (2.4.7)$$

Furthermore, field emission (FE) current by tunneling increases exponentially with high doping concentration, where the depletion zone is reduced. The thermionic field emission (FTE) is a transport mechanism due to both medium doping concentrations and thermally induced current. The contribution of these transport mechanisms can cause an increase of current density in metal-semiconductor junction (see Figure 2.4.4).

Hence, a metal-semiconductor junction can form an ohmic contact when exists conduction in both direction with very little voltage drop. This is achieved when the potential barrier and depletion zone are reduced.

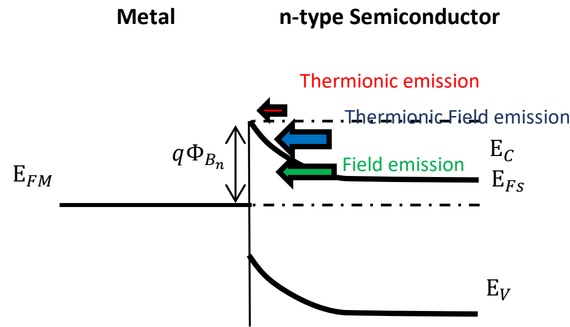

Figure 2.4.4 Different types of conduction mechanism that can exist in a metal-n-type-semiconductor junction.

2.4.2 Van der Pauw method

One of the methods used to measure the resistivity on materials (conductor and semiconductors) is the Van der Pauw method [40]. This method uses four tips, which are in contact with the surface of the sample. The tips are locating at the boundary of the sample, injecting current by two adjacent tips and measures the voltage with the other pair of tips (see Figure 2.4.5). The van der Pauw allows to measure samples of arbitrary shape with high precision when the following conditions are satisfied [40]:

a) The sample quality has to be homogenous and its thickness must be constant.
b) The contacts must be placed at the edges of the sample.
c) The sample must not have isolated holes.
d) The area of contact between the tips and the sample should be sufficiently small.

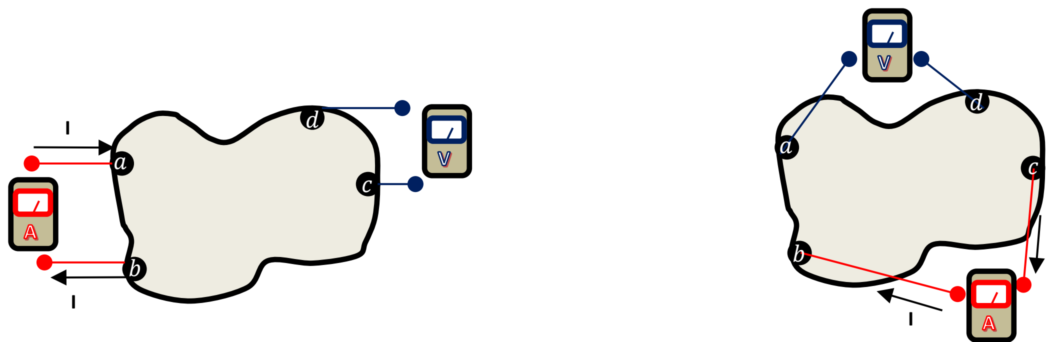

Figure 2.4.5 Electrical configuration for Van der Pauw method. Left side represents the configuration to obtain the $R_{ab,cd}$ and right side represents the configuration to obtain the resistance $R_{bc,da}$.

Van der Pauw established a general relationship, shown in equation 2.4.8. Here $R_{ab,cd}$ is the characteristic resistance that is equal to the potential differences between contact a and b divided by the current passing through contacts c and d, $R_{bc,da}$ is the characteristic resistance that is equal to the potential differences between contact b and c divided by the current passing through contacts d and a, t is the thickness of thin film and ρ is the electrical resistivity of the sample [41].

$$e^{\frac{t\,.R_{ab,cd}}{\rho}} + e^{\frac{t\,.R_{bc,da}}{\rho}} = 1 \tag{2.4.8}$$

2.5 Structural properties of amorphous semiconductors

Both electrons and molecules in a solid can absorb light, for the case of infrared spectroscopy at energies between 0.001-1.7 eV, the molecules only absorb energy at a certain frequency which coincides with their natural vibrational frequency that allowed transitions between pairs of energy levels. In addition, this absorption happens due to the dipole moments changes, which can be subdivided into two classes, depending on whether the bond length and angle is changing: stretching (symmetric and asymmetric) and bending (rocking, wagging, scissoring and twisting) of an asymmetrical nature as is see in Figure 2.5.1 [42][43]. The symmetrical bonds cannot be detected by infrared spectroscopy, as they do not possess a net change in dipole moment. The symmetrical vibrations are usually active in a Raman spectrum. In addition, a “shift” of vibration frequency can occur due to the effects of the nearest neighboring atoms [44][45].

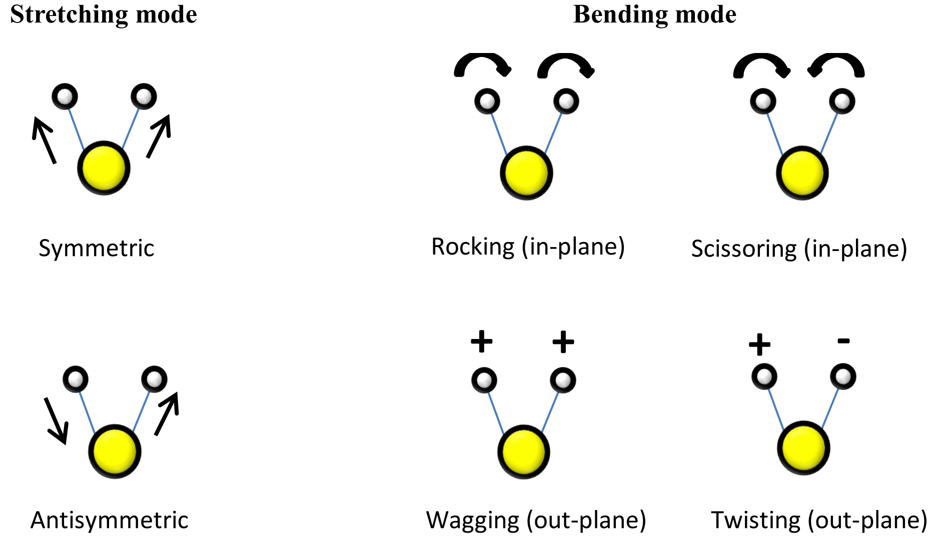

Figure 2.5.1 Stretching and bending modes of molecular vibrations.

In order to determine the absorption coefficient in this case, it makes use of Lambert-Beer's Law as shown in the equation (2.4.1.1), where $\alpha(\nu)$ is the absorption coefficient and ν is the wavenumber, T is the transmittance related to the absorption due to the distinct vibrational modes in the material while T_0 is the zero-absorption transmittance. The number of bonds density N related to the absorption peaks can be estimated through the equation (2.5.1) knowing the corresponding (k) inverse absorption cross section for each vibrational mode [46]. In this way, it is possible to monitor the variation of the number of distinct bonds.

$$\alpha(\nu) = \log\left(\frac{T}{T_0}\right)/d$$
$$N = k\int\frac{\alpha(\nu)}{\nu}d\nu \qquad (2.5.1)$$

On the other hand, it is possible quantify the hydrogen concentration $[H]$ through the hydrogen-related bond density (see equation 2.5.2). Here $\nu_i(\alpha)$ is the wavenumber and the sub-index represents the different types of hydrogen-related bonds [47].

$$[H] = \sum_i N_i = \sum_I k_i\int\frac{\alpha_i(\nu)}{\nu_i}d\nu_i \qquad (2.5.2)$$

Experimental Details

3.1 Deposition

The *a*-SiC:H films were grown on double side polished fused silica (SiO_2) and polished silicon (Si) substrates by radio frequency magnetron sputtering using a high purity SiC target. The pressure before the deposition process was below 2×10^{-6} mbar. The distance between the target and the substrate ranged from 1 cm to 3 cm. The substrates were cooled down with a constant water flux at 12 °C to ensure the amorphous structure of the films. Nevertheless, the substrate temperature reached up to ∼50 °C during the deposition. Before deposition, the targets were pre-sputtered for 30 minutes in order to eliminate superficial contamination resulting from exposure to air. In the case of the *a*-SiC:H(Al) films, the deposition was performed in an argon-hydrogen atmosphere mixture using a high purity SiC and aluminum target. The typical power used to get a suitable amount of Al in the layer is 10 Watts. In the case of the *a*-SiC: H(Al) grown with different Al amounts, a single process was performed with the configuration of magnetrons and sample holder (see Figure 4.1.1). The deposition conditions are listed in Table 3.1.

Table 3.1. Deposition table

Sample- Date	Ar-H_2 flow (sccm)	Power SiC (Watts)	Power Al (Watts)	Time (min)	Distance Target-substrate (cm)	Pressure before deposition (mbar)	Pressure after deposition (mbar)
S1 – 12/03	27-3	140	-	300	3	$1.29\text{x}10^{-6}$	$1.12\text{x}10^{-6}$
S2 – 19/03	27-3	140	-	600	3	$1.13\text{x}10^{-6}$	$7.44\text{x}10^{-7}$
S3 – 04/04	27-3	140	8	480	3	$1.37\text{x}10^{-6}$	$1.26\text{x}10^{-6}$
S4 – 21/04	27-3	140	5	600	2	$1.29\text{x}10^{-6}$	$1.12\text{x}10^{-6}$
S5 – 28/05	27-3	140	10	300	1	$1.44\text{x}10^{-6}$	$7.41\text{x}10^{-7}$

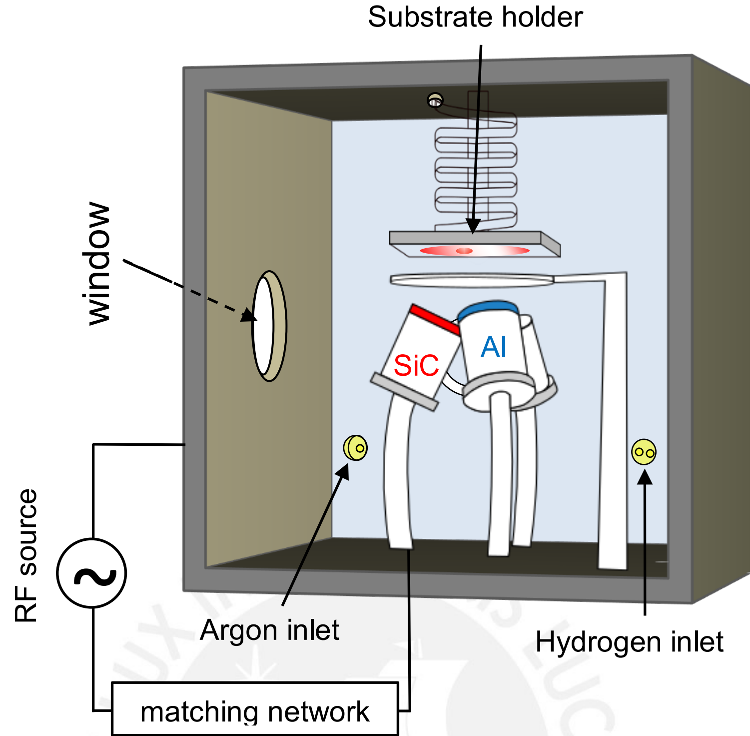

Figure 4.1 Magnetrons arrangement in order to obtain a gradient of aluminum concentration on the *a*-SiC:H films. The image shows SiC and Al target fixed on the surface of the magnetrons. The substrate is fixed to a movable substrate holder with active cooling in order to ensure the amorphous state of the layer. Argon gas is introduced in the chamber when is in high vacuum and afterwards, an electric RF-field with a frequency of 13.56 MHz is applied through the target in order to form a plasma that allows removal of atoms from the surface of the targets towards the substrate.

3.2 Optical characterization techniques

UV-VIS transmittance

Transmission spectroscopy in the visible, infrared and ultraviolet range is used because it allows characterize thin and thick films in the range from few hundreds to thousands of nm, determining its optical parameters, such as refractive index, absorption coefficient and thickness [48]. For this purpose, the substrate must be transparent in the UV / VIS / IR range. The samples were grown on fused silica SiO_2 substrates were characterized via UV / VIS spectrophotometry in the Center for Materials-Characterization

(CAM) at the PUCP. The used equipment was a double beam photo-spectrometer model Lambda 2-950 UV/VIS/NIR from the company Perkin Elmer. The measurements were made in a spectral range from 190 nm to 1500 nm and with a step of 1 nm between each measurement.

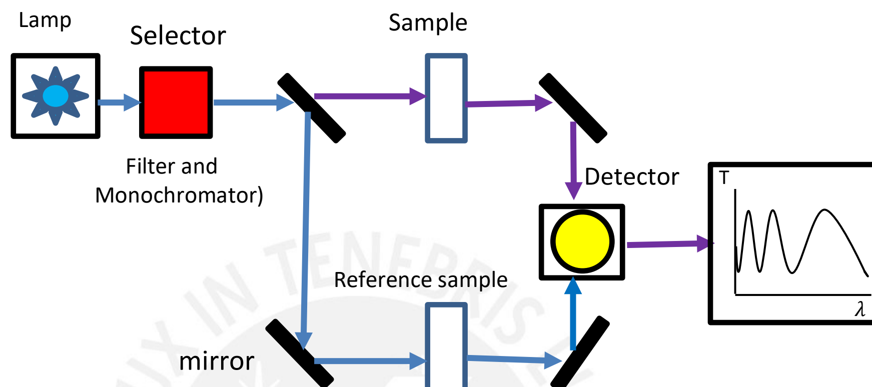

Figure 3.2.1 Schematic of UV-visible spectrophotometer work. The optical transmittance is determined by measuring the passing light intensity across the sample and the light intensity across air only.

The sample receives electromagnetic radiation that is absorbed or transmitted depending on the wavelength of the radiation wavelength and the optical constants of the material. The radiation absorbed is that with the energy necessary to excite the valence electrons by changing their energy state, this will depend on the bandgap of the material. The spectrophotometer is a dispersive-type optical instrument used to measure transmittance; its schematic is shown in Figure 3.2.1. This instrument is composed of two light sources with light sources: a tungsten lamp for the ultraviolet and visible range, and another deuterium lamp for the near-infrared range. Another part is the monochromator that selects the wavelength, works as a scattering element, and an optical system for light collimation on the sample. Finally, a sample holder, light detector and a reading system are required for the signal detected. The light leaves the source and passes through a monochromator that selects a very small range of wavelength (selector). A first measurement is made without placing any sample, taking as reference the air and then a

second measurement is made with the sample. The recorded signal is the quotient between the signal with the sample and the reference. When there is no sample, the transmission detected by the spectrophotometer reaches 100 %, so that when the spectrum is taken with the sample, the percentage of transmission T (λ) is obtained as the quotient of the detected signal with respect to the obtained for the background at each wavelength value (λ) as shown in Figure 3.2.2.

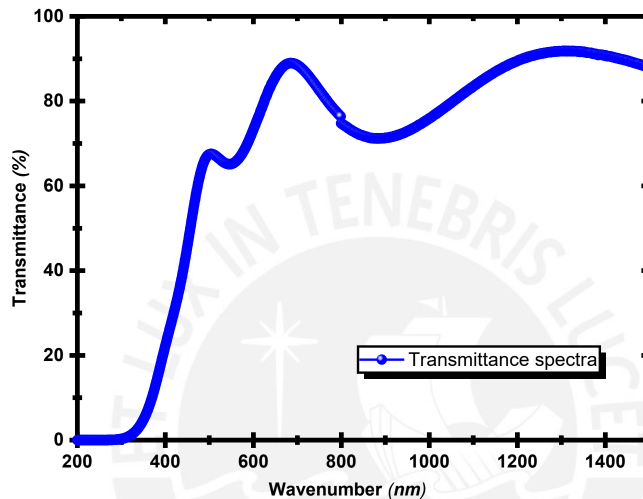

Figure 3.2.2. Transmittance spectra of S5-sample at wavelength range from 200 nm to 1500 nm.

3.3 Structural characterization

Infrared absorption by Fourier transform spectroscopy (FTIR)

Infrared transmittance measurements taken on the amorphous films were carried by using an infrared spectrometer Tensor 27 from the company Perkin Elmer. An example of the measured transmittance is shown in Figure 3.3.1. The measurements were a performance with a resolution of 8 cm^{-1}. These spectra were recorded in the spectral region from 400 cm^{-1} to 4000 cm^{-1} and were corrected for the silicon substrate absorption. All these spectra were normalized by an uncoated silicon substrate spectrum and corrected with background signal due to interference fringes by the thickness of the layers.

The basic components of the FTIR spectrometer are shown in Figure 3.3.1. These are a source of infrared light, an interferometer and a detector. The IR radiation of the

source is directed to a beam splitter, which is divided in into two beams, a part of the light is reflected towards a fixed mirror and the other is transmitted to the moving mirror. Then, the reflected return beams are superimposed and separated by a beam splitter, one goes back towards the source and the other is directed to the sample. The moving mirror produces an optical path difference (OPD) between two arms of the interferometer. When the distance between the beam splitter and fixed mirror are equal, the OPD is zero, which causes constructive interference and maximum intensity. The resulting signal, the light intensity I versus mirror position x, has all spectral information that comes from the source. Finally, the beam leaving the interferometer passes through the sample and the intensity I(x) modified by the sample is measured by the detector.

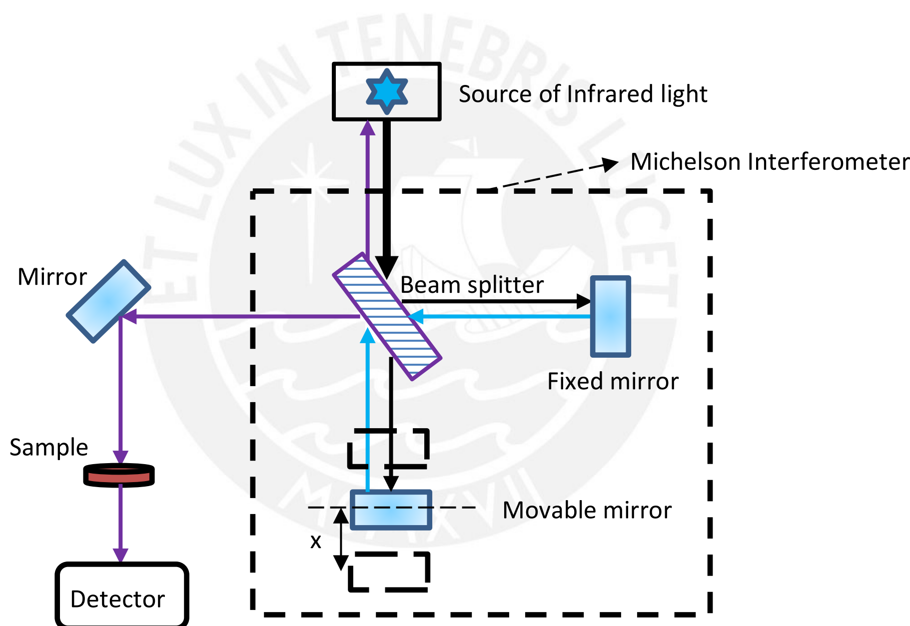

Figure 3.3.1 Schematic diagram of an FTIR spectrometer

Electrons in a solid are not the only ones that can absorb light. The molecules can absorb light too. This radiation must be able to excite the bonds present in the solid. The IR absorption spectra provide information on the molecular bonds; thus, IR spectra is a fingerprint for the material. The FTIR uses a Michelson interferometer, which allows to

transform from time to frequency domain and builds the infrared spectrum. As shown in Figure 3.3.2.

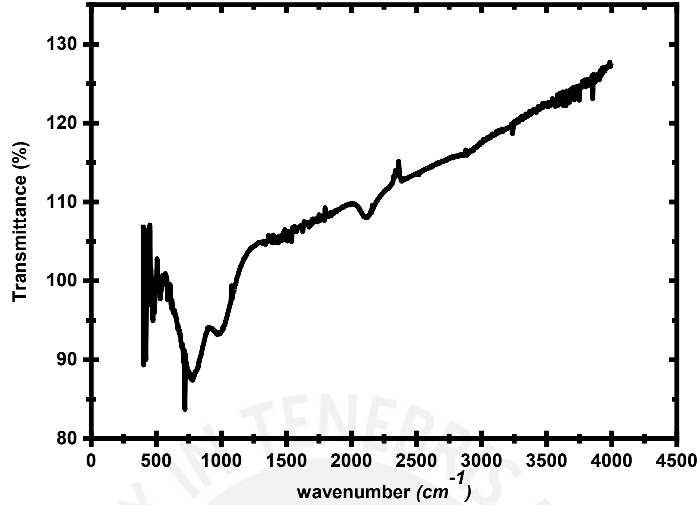

Figure 4.3.2. Typical IR transmittance spectra of SiC thin film grown on silicon. The substrate absorption is corrected by using an uncoated Silicon substrate as reference.

Raman spectroscopy

Raman measurement taken on the amorphous films were carried out by using a Renishaw in-Via Reflex Spectrometer. A schematic of the experimental setup is shown in Figure 3.3.2 with an Argon laser whose wavelength is 514.5 nm and 488 nm used as a source of excitation. These spectra were recorded in the spectral region from 102 cm^{-1} to 3200 cm^{-1} with a step of 3 cm, a resolution of 4 cm^{-1} and a slit of 2400 $lines.mm^{-1}$.

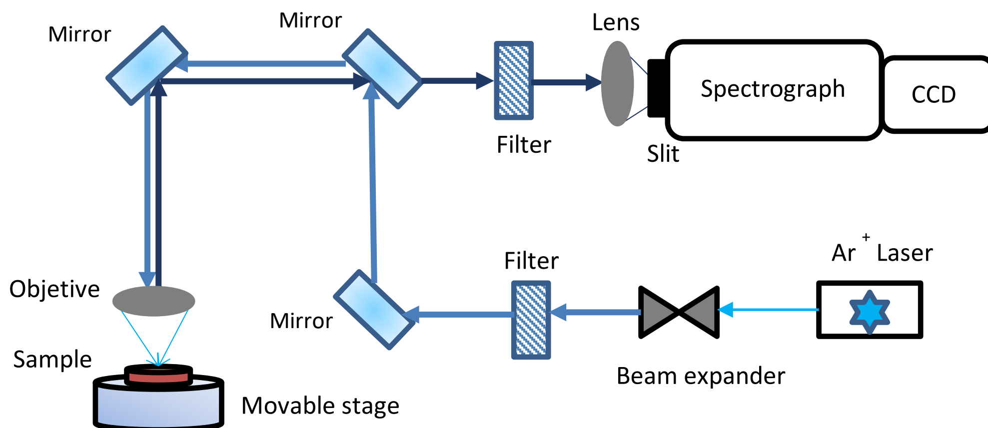

Figure 3.3.2 Schematic diagram of the Raman system modified scheme of [49].

Figure 3.3.2 shows a schematic diagram of the Raman system. It is made up of an Argon ion laser source, the beam passes through a beam expander, filters and mirrors until it reaches an objective lens, which concentrates the light on the sample. Then, the light scattered by the sample is conducted to a monochromator, which is responsible for separating the spectral components and finally, the photons from the monochromator are converted into an analogue signal by the detector (CCD: Charge-coupled device), which are then digitized and displayed on a computer.

Raman spectroscopy is a vibrational spectroscopic technique and non-destructive that is used to provide molecular information, such as the relative quantity of crystalline at the amorphous phase is in thin films bulk materials [50].

Raman spectra are obtained when light is irradiated with a laser on a sample and this scatters photons in two ways, elastic and inelastic scattering, known as Rayleigh scattering and Raman scattering respectively.

In the elastic scattering the system goes from a basal energy level to an excited one, when it relaxes, it returns to the initial basal level and emits a photon with the same frequency as the incident. Whereas, inelastic scattering, the system doesn't return to the original energy level (which can be the basal or an already excited state). Here, the energy level reached after relaxation can be higher (Stokes scattering) or lower (anti-Stokes scattering) at the initial level. From this, in a Stokes scattering, the photon emitted after relaxation has a

frequency lower than that of the incident photon, while in an anti-Stokes scattering the photon emitted has a higher frequency than the photon incident [51] as shown in Figure 3.3.3.

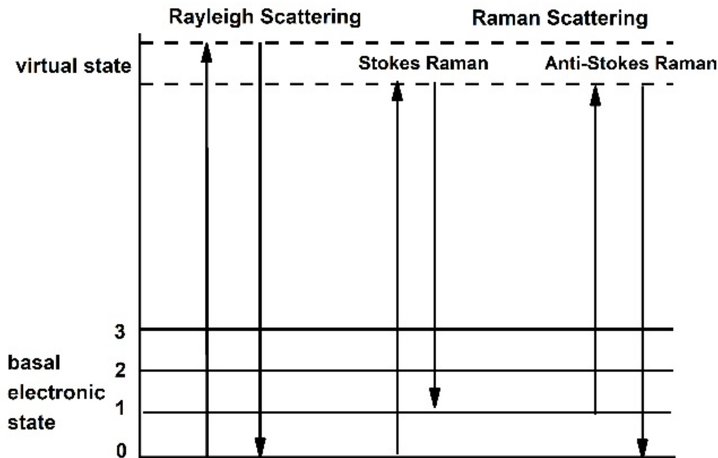

Figure 3.3.3 Diagram of electronic processes that give rise to Rayleigh and Raman scattering. Modified scheme retrieved from [8].

Energy dispersion of X-Rays Spectroscopy

Energy dispersion of X-Rays Spectroscopy (EDX or EDS) is a technique that uses physical analysis for quantitating characterization of the element composition of a sample. Element compositional of the samples were measured using an SEM Model JEOL JSM-7610F equipped. In Figure 4.3.4 show a schematic diagram of the main component of the sample mode by SEM.

Its source of emission is a hot filament which electrons are accelerated. Usually, the filament is tungsten that uses the thermionic emission. At temperatures above 2700 K emits a large number of electrons, where they tend to accelerate through a variable potential difference between 1- 40 kV. The electron beam produced by two or three stages of magnification by condenser lenses tends to accelerate to form a parallel beam. The

diameter of the electron beam is 2- 10 nm. An X-ray detector captures this type of signal, from which a spectrum of elements is obtained, that is, elemental chemical analysis of the sample. The signal is detected by several kinds of detectors, which allow to capture the result of the interaction of the electron beam with the sample and transform it into an electrical signal. This entire system is connected to a turbo molecular pump to generate the vacuum.

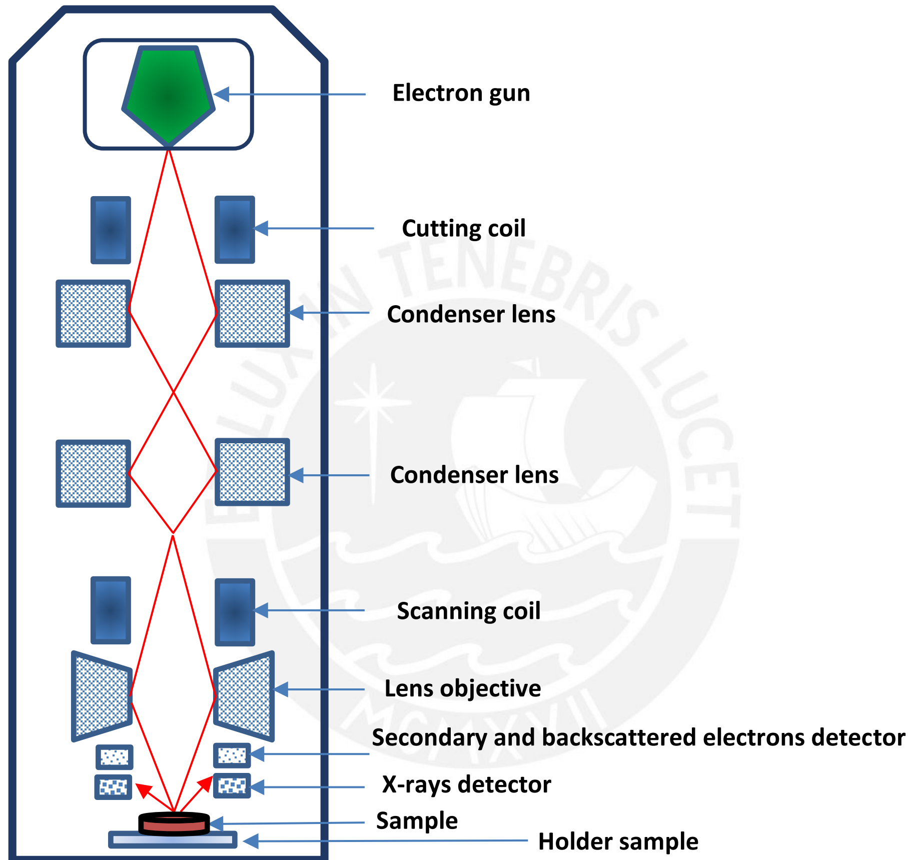

Figure 3.3.4 Schematic diagram of EDS main components.

Furthermore, all EDS spectra were measured using the same conditions, such as an acceleration voltage of 4 kV. It is important to use an adequate acceleration voltage to do not take into account the substrate (silicon) signal. In addition, the working distance was 10 mm, a magnification of 400 X and quantification time was 500 s.

The EDS system detects X-Rays emitted by the sample in response to being hit with electrons emitted by an electron beam of a Scanning Electron Microscopy (SEM), thus an EDS system is commonly coupled with an SEM system.

Its characterization capabilities are based on the fundamental principle that each element has a unique structure allowing X-rays that are characteristic in an element atomic structure to be identified uniquely from each other.

The X-Rays are caused by the beam of electrons hitting the sample. This interaction may excite an electron of an inner shell, ejecting it from the shell while creating a hole where the electron was. An electron from outer, high energy *shell* then fill the hole, and the difference between high energy shell and lower energy shell may be released in the form of characteristic X-Rays. Furthermore, in this interaction, elastic and inelastic dispersion signals are also generated. In the inelastic dispersion, the electrons lose part of its energy, but without suffering a significative deviation of its trajectory, thus the ejection of this electron is called Secondary electron (SE). In the elastic dispersion, the electron not significative loses its energy, but suffers a change in the direction of its trajectory, this electron is called backscattering electrons (BSE) [52]. All the phenomena that occur when the electrons ejected on a sample are shown in Figure 3.3.3.

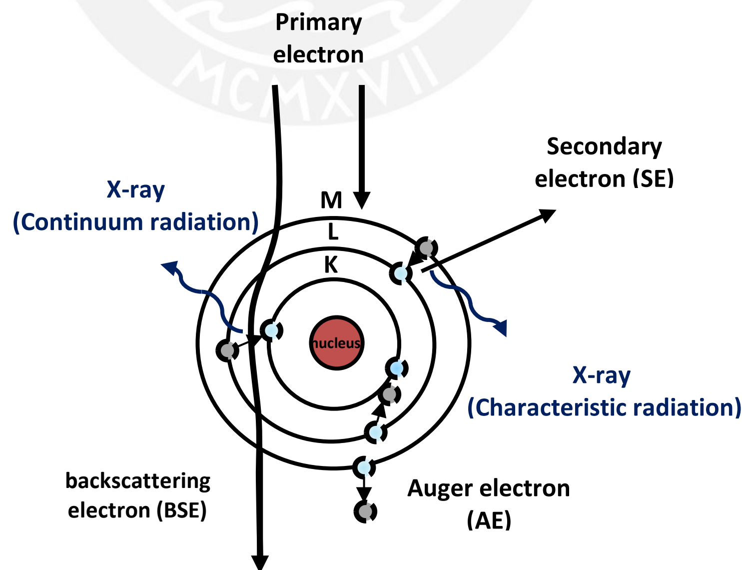

Figure 3.3.5 Phenomena that occur in the electron-sample interaction. Scheme taken an modified from [52].

X-Rays Diffraction (XRD)

X-Rays Diffraction is a non – destructive technique used to determine the crystalline, structure properties of the material. In addition, it allows the differentiation of crystalline, polycrystalline and amorphous structures. Diffractograms were determined using a D8 Discovery from the company Bruker whose schematic is shown in Figure 3.3.6 at a voltage 40 kV and a current of 40 mA, using $Cu\ K\alpha$ radiation source ($\lambda = 1.5418$ Å). Diffraction angles (2θ) were detected in a range of 5 ° to 70 ° using a step of 0.02 ° with a total time of 570 s.

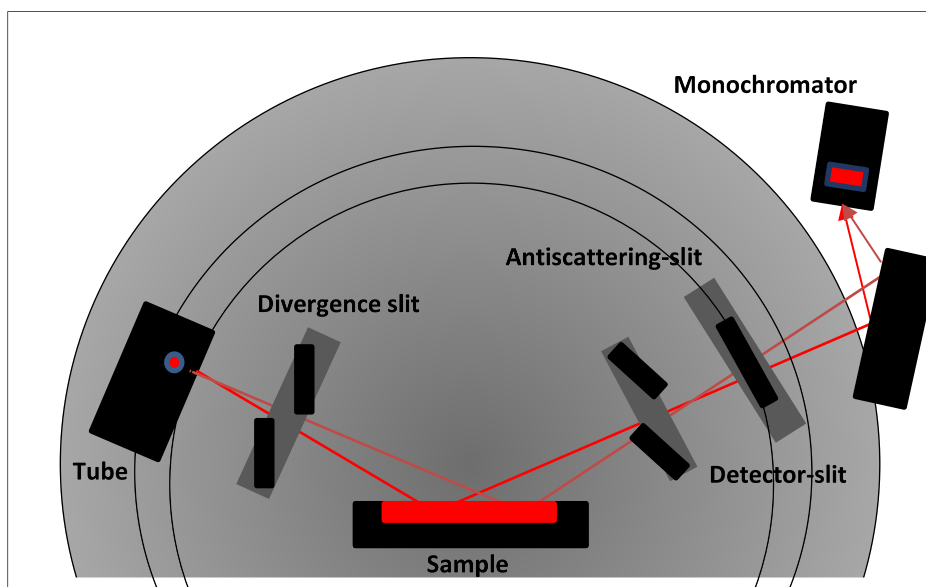

Figure 3.3.6 Schematic Bragg-Brentano setup used in the D8 Discovery from Bruker.

Mass spectrometry (MS)

Mass spectrometry is an analysis technique that enables a direct identification of molecules based on the mass-to-charge ratios. These spectra of the samples were measured using a Prisma Plus Quadrupole Mass Spectrometer [53]. This spectrometer is connected directly to Sputtering chamber as shown in Figure 3.3.7. The Quadera software is connected to the mass spectrometer to transfer all measured data. These measurements were made before and after the sputtering process to verify impurities.

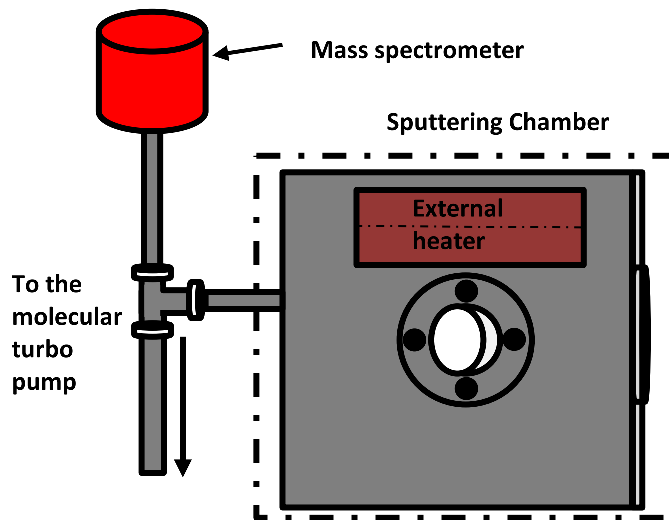

Fig.3.3.7. Mass spectrometer diagram connection (lateral view).

A tungsten filament produces high energy electrons in order to ionize molecules of the gas inlet of the chamber at a lower pressure below $1 \times 10^{-4}\ mbar$ (the ion source). These ions are sorted and separated according to their mass and charge by electric and magnetic field perturbation (the mass filter analyzer). The separated ions are then measured, and the result is displayed on a chart (Faraday-detector). The working principle of the device was schematized in Figure 3.3.8.

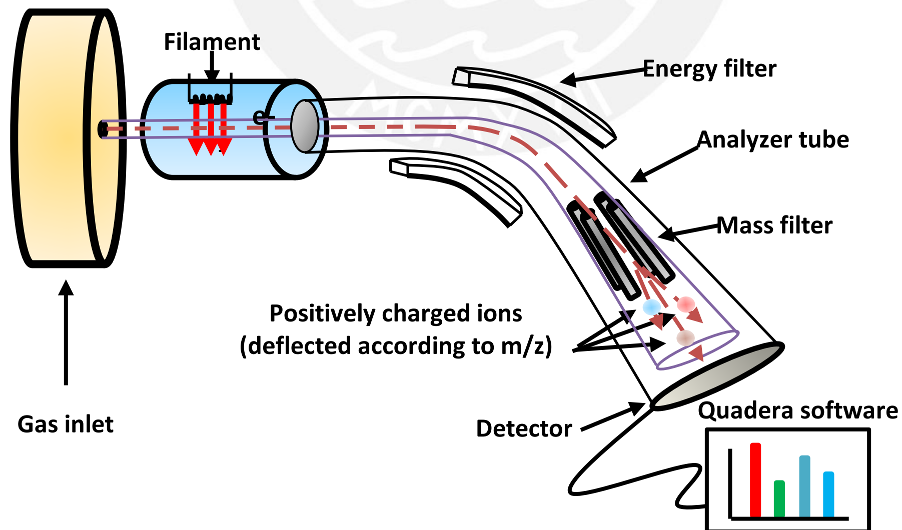

Figure.3.3.8 Schematic diagram of mass spectrometer.

3.4 Electrical Characterization

Van der Pauw technique

The Van der Pauw is one of the most effective and widely used techniques of the four-probe methods for measuring the resistivity of a thin film having an arbitrary shape [40]. Four probes methods are probably the most outstanding due to that they are not susceptible to the effects of the resistance of the cables and the contacts between the electrical contact and sample, thus allowing a more accurate and reliable result [54].

Before measurement the resistivity of the samples, we need to deposited metallic contacts on the corners of the perimeter of the sample. Aluminium contacts were deposited in order to guarantee the contacts between the tip and sample which allow the flux of current across the film and Titanium contacts were deposited on Aluminium in favour of high wear resistance. The contacts were deposited by radio frequency magnetron sputtering using two targets of Aluminum and Titanium respectively using pre-designed masks. These depositions took place in the Center for Micro-and Nanotechnologies (ZMN) of the TU-Ilmenau. The deposition parameters are listed in Table 3.4.

Table 3.4. Deposition table of metallic contacts

Sample- Date	Power Al and Ti (Watts)	Thickness Al (nm)	Thickness Ti(nm)	Al-Ti time deposition	Pressure(mbar)
S5 – 28/05	100	20	200	23 s – 474 s	$5.7x10^{-7}$

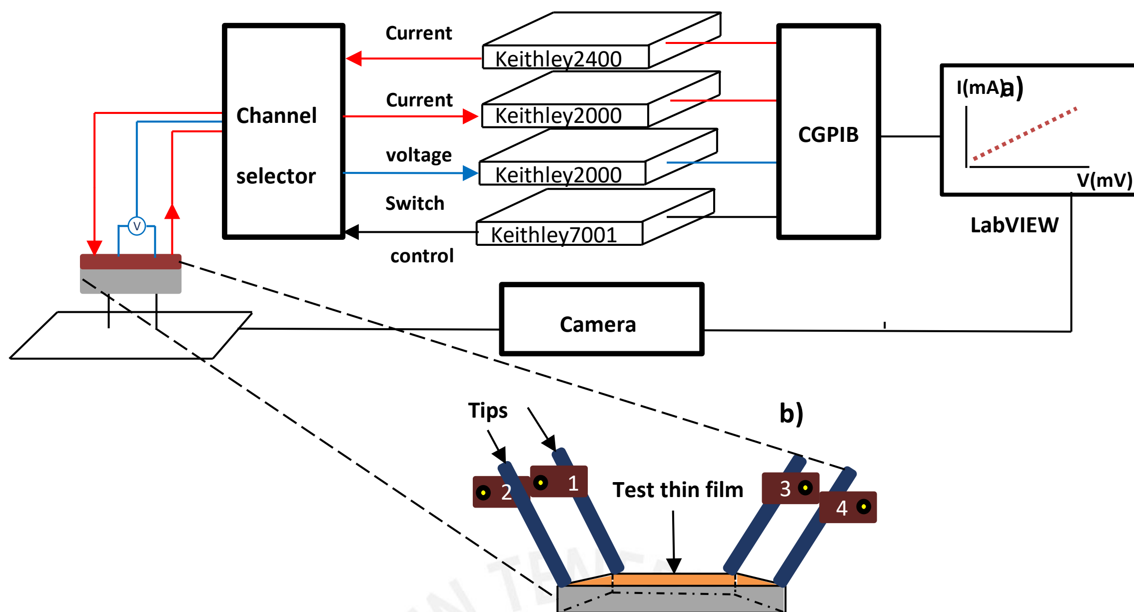

Figure 3.4 Interconnection diagram for van der Pawn measurement (a) Setup of the tips on sample (b).

The electrical resistivity was measured by using a Keithley 2400 Source Meter, Keithley 2000Multimeter, Keithley 2001Multimeter, Keithley 7001 Switch/control system, all connected through the GPIB and a camera. LabVIEW interface interacts with the devices previously mentioned. The I-V diagram is plotted on the interface. It offers the possibility to obtain the resistance of the sample. The interconnection between the Keithley devices and the channel selector is shown in Figure 3.4 (a). Whereas the setup of the tips on samples is shown in Figure 3.4 (b).

3.5 Annealing treatments (Rapid thermal Annealing)

The Rapid thermal annealing is considered a more positive annealing method than furnace annealing due to it can be improving the microstructure and electrical properties [55]. It was performed on Jipelec Jetstar 100 RTP furnace, located at the Center for Micro- and Nanotechnologies (ZMN) at the TU-Ilmenau. The schematic diagram of the RTP system is shown in Figure 3.5.1. The system consists of a halogen lamp arranged on the top serving as heat sources. The sample was annealed in an argon atmosphere. The sample was placed on a wafer holder and its temperature read through a pyrometer placed below the wafer. The chamber is cooled by enclosed circulating water and thus referred

to as a cold wall chamber. After the operating system temperature was reached, the samples were moved rapidly inside the oven for 600 seconds to then it leaves cooling at room temperature. This procedure was carried out for the same film by varying the temperature from 200 °C to 600 °C. The heating rate for the temperature of 200 °C, 300 °C, 400 °C and 600 °C were 8.7 °C/s, 14.0 °C/s, 18.9 °C/s and 28.9 °C/s respectively. The reason for all these different annealing treatments is to study how they affect their structure, their electrical and optical properties. The temperature-time profile used for treating the samples is shown in Figure 3.5.2.

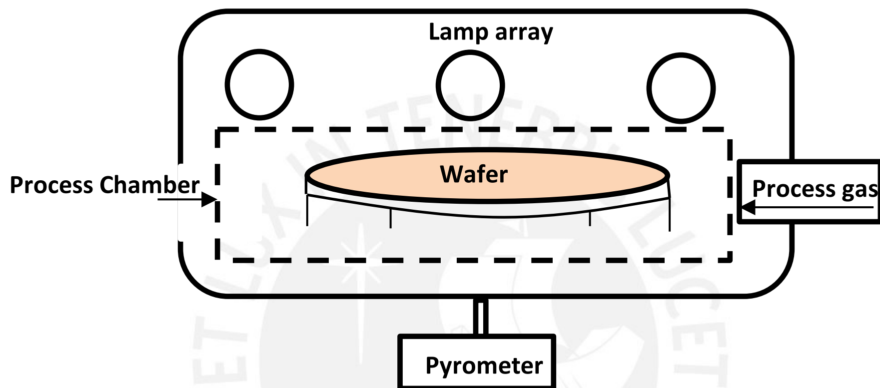

Figure 3.5.1 Schematic diagram of the rapid thermal processing system.

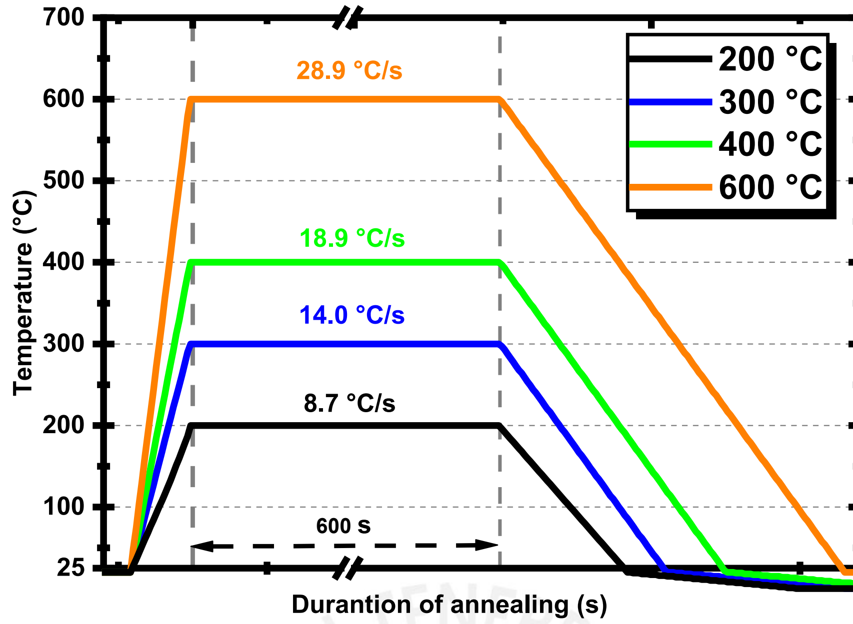

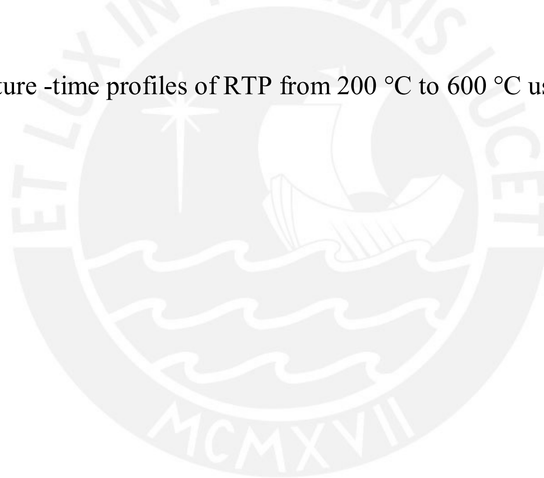

Figure 3.5.2 The temperature -time profiles of RTP from 200 °C to 600 °C used in this work of SiC-like (Al).

4. Result and discussion

4.1 Chamber conditioning

In order to find the appropriate parameters to produce Aluminum doped hydrogenated amorphous silicon carbide (Al doped-*a*-SiC:H) thin films and to achieve a high reproducibility, depositions of five samples were made. In addition, a reduction of the humidity within the chamber was obtained. For this purpose, some heaters were installed externally to the chamber. The chamber was heated previously the deposition process.

Prior to analyzing the FTIR spectra of the produced SiC thin films, the elemental composition of each sample was determinate by SEM-EDS. All measurements were performed applying the electrons beam at the center of samples. As it was expected, each sample reveals elements as silicon, carbon, along with other elements such as oxygen and aluminum. The elemental atomic concentration of the samples is listed in Table 4.1.1.

Table 4.1.1. Elemental atomic concentration of samples produced before and after sequentially heating the chamber. Here N.D means not detected.

Sample- date	Matrix	Chemical formula	Al (at. %)	Si (at. %)	C (at. %)	O (at. %)
S1-12/03	SiO_2-like	*a*-SiCO:H	-	-	-	-
S2-19/03	Si-C-O	*a*-$SiC_{0.97}O_{0.25}$:H	-	44.99	43.79	11.22
S3-04/04	Si-C-O(Al)	*a*-$SiC_{1.12}O_{0.28}$:H(Al)	N. D	40.95	46.06	11.79
S4-21/04	SiO_2-like (Al)	*a*-$SiC_{0.23}O_{1.47}$:H(Al)	N. D	37.02	8.47	54.51
S5-28/05	SiC-like (Al)	*a*-$SiC_{0.95}O_{0.13}$:H(Al)	0.31	47.9	45.36	6.43

The effect of implementing the heaters on the quality of the SiC thin films composition can be seen in the FTIR measurements shown in Figure 4.1.1. As mentioned in the third chapter, FTIR spectroscopy allows the identification of different types of bonds through the peaks in the characteristic frequency of vibrations modes. The presence of oxygen-related bonds for different depositions after implementing the heaters in the chamber assessed.

In this section, we evaluate the evolution of the oxygen-related peaks position from the FTIR spectra and the bond density of silicon-oxygen as well. The spectra exhibit two regions. The first located between 400 cm^{-1} and 1300 cm^{-1}, in which the Si-C (760 cm^{-1} – 816 cm^{-1}), Si-CH

(980 cm^{-1} -1000 cm^{-1}) and Si-O_x (1040 cm^{-1} -1220 cm^{-1}) vibrational modes can be found. The second zone between 1500 cm^{-1} and 3300 cm^{-1}, in which the Si-H (2000 cm^{-1} – 2200 cm^{-1}) and CH_x (2800 cm^{-1}– 3200 cm^{-1}) vibrational modes are observed (See Table 4.1.2).

The samples were growing with different periods in order to analyze the evolution of the Si-O bond number density. Using 2.5.1 equation to baseline subtraction and thickness normalization of infrared absorption spectra of all thin films. These spectra are shown in Figure 4.1.2.

Table 4.1.2 Summary types vibration modes and their corresponding frequency (cm^{-1})

Vibrating mode	SiC-like	Si-C-O	SiO_2-like
Si-O-Si *rocking* [13]	…	450	440
Si-C *stretching* [56]	780	800-815	…
Si-O *bending* [42]	…	…	820
Si-CH_x *wagging* [57]	998	994	…
Si-O *transverse optical* [42]	1107	1062	1020
Si-O *longitudinal optical* [58]	…	…	1144
Si-H_x *stretching* [59]	2000-2200	2000-2100	2000-2100
C-H_n *stretching* [59]	2800-3000	2800 -3000	…

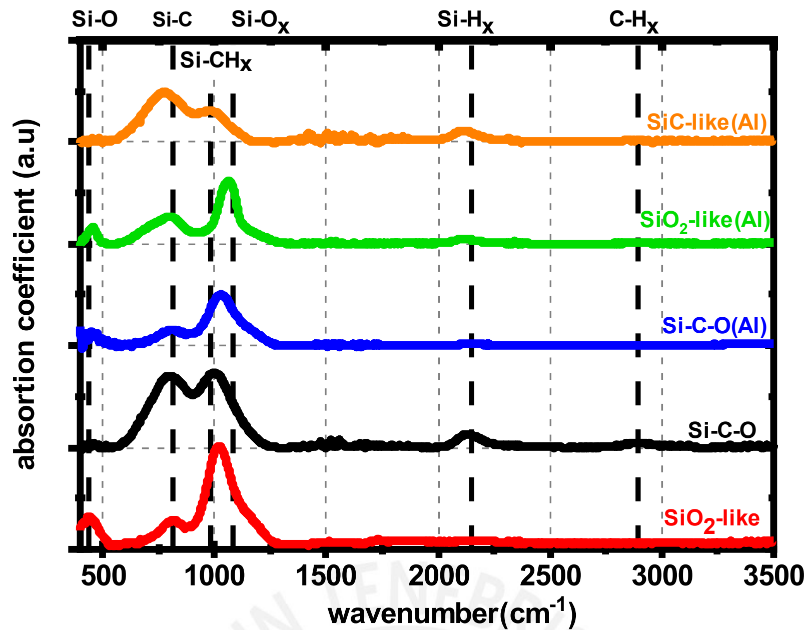

Figure 4.1.1 IR absorption spectrum over 400 cm^{-1} – 3500 cm^{-1} of samples at different time deposition. The spectra are vertically displaced and normalized for the sake of clarity only.

FTIR measurements reveal the formation of not only about Si-C bonds but also Si-O bonds. The main vibration modes occur in the first zone located between 400 cm^{-1} and 1300 cm^{-1}. The spectra of the first two samples without aluminum doping are evaluated. In Figure 4.1.1 the peaks around 1040 cm^{-1} and 1220 cm^{-1} corresponding to Si-O vibrational modes are in the samples [58], which implies the presence of oxygen on the samples. The samples without aluminum doping show a decrease of intensity around the 1040 cm^{-1} and the 1220 cm^{-1}. This decrease is accompanied by an existing decrease in peak intensity around 460 cm^{-1}, that is related to Si-O rocking vibration mode. In addition, there is a peak around 816 cm^{-1}in the IR absorption spectrum of the sample labelled Si-O_2-like which corresponds to the Si-O vibrational mode accordance with *Gallis et al* [56]. While Si-C-O sample shows a peak around 993 cm^{-1}, that corresponding to C-H_x group attached to Si atom vibrational mode. There is a decrease in the peak around 1220 cm^{-1}, this peak is very weak to compare to that at 1040 cm^{-1}, as well [7][58].

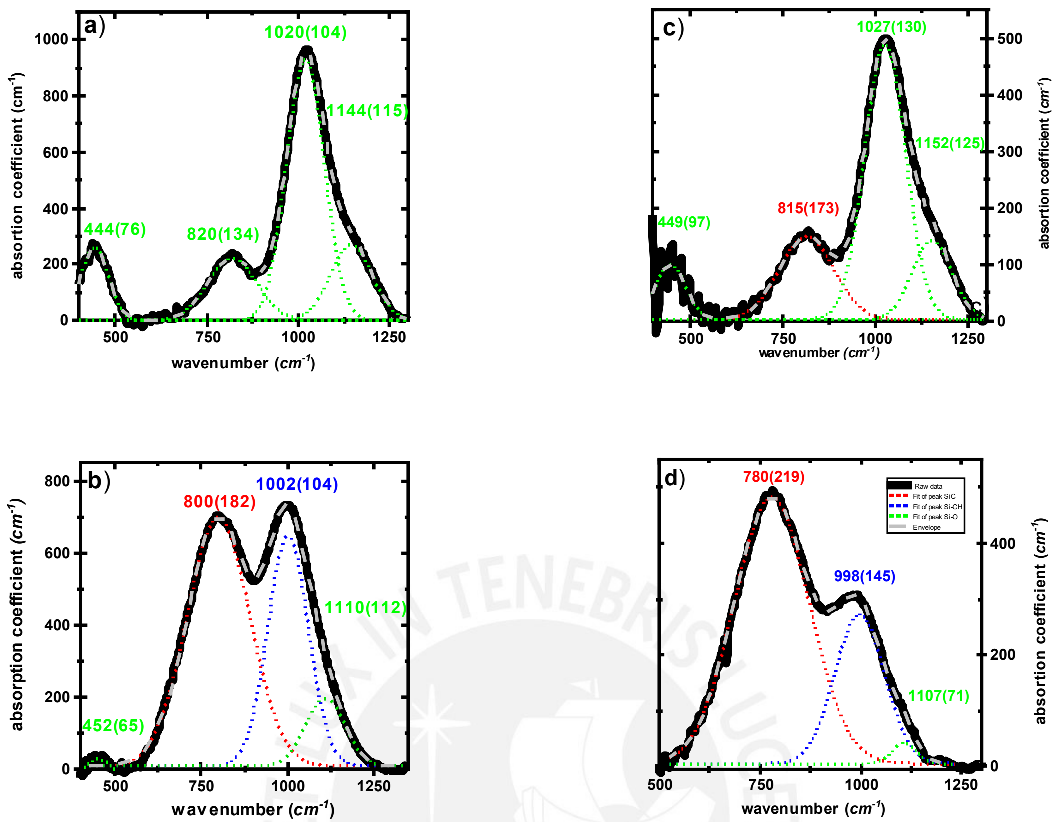

Figure 4.1.2 Multi-peak fit of the infrared absorption band from 400-1300 cm^{-1} a) SiO_2-like, b) Si-C-O, c) Si-C-O(Al), d) SiC-like (Al) samples. Green curve gaussians are associated with Si-O bond, blue curve is associated with Si-(C-H)$_x$ bond and red curve is associated with Si-C bond. Theoretical envelopes (sum of deconvoluted bands) are given by grey dash. The experimental curve is given by thick black line.

The spectra of samples with aluminum doping are evaluated as well. In the IR absorption spectra of Si-C-O(Al) and SiO_2-like (Al) samples, Si-O bonds are also observed. The incorporation of higher Oxygen concentration into the films results in a shift the Si-C stretching mode toward higher wave numbers. This shift is accompanied by a rise in the intensity of the Si-O stretching mode. The latter suggests the presence of a suboxide phase. In Figure 4.1.2 the SiC-like(Al) sample presents a shift to a lower wavenumber of a peak that corresponds to Si-C bond in comparison to the other samples and the shoulder appearing around 1000 cm^{-1} is attributed to the rocking and wagging vibration mode of the C-H_x group attached to the silicon [60]. In order to better observe the displacements of each vibration mode and to obtain the evolution of the bond density of Si-O

bonds, a deconvolution was made with Gaussian curves on the vibration modes. These curves were used due to the amorphous nature of the samples.

The employed inverse absorption cross-section at the Si-O bonds [Table 4.1.3] in the 3.3.2 equation is shown in Figure 4.1.2 and Figure 4.1.3.

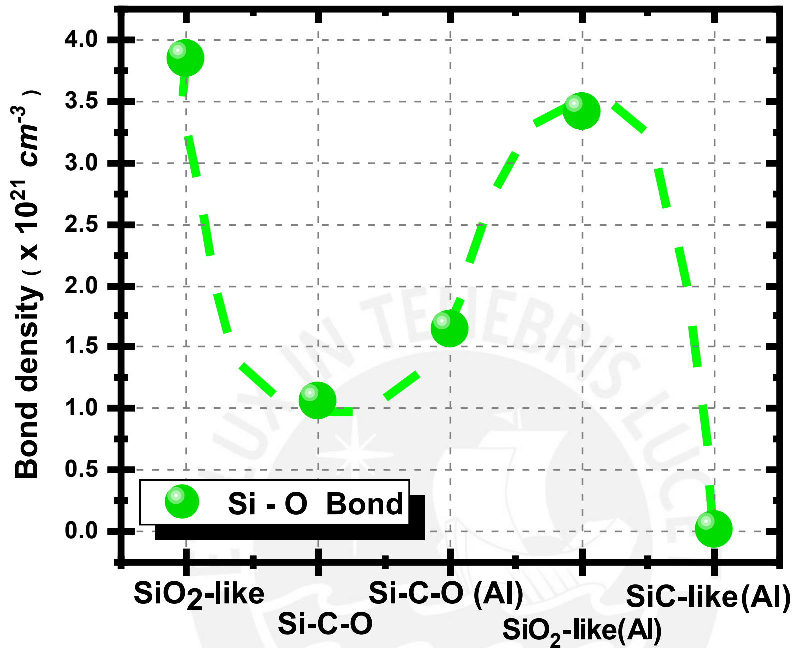

Figure 4.1.3 Calculated Si-O bond density for absorption peak obtained from FTIR spectral versus samples deposited through of time.

Table.4.1.3 The values of inversion absorption cross-section

Si-C (cm^{-2})	Si-O(cm^{-2})	Si-H(cm^{-2})	C-H(cm^{-2})	References
$\mathbf{2.13 \times 10^{19}}$	1.50×10^{19}	$(1.4 \pm 0.1) \times 10^{20}$	$(1.35 \pm 0.35) \times 10^{21}$	[57][61]

As another observation, the samples with lower Si-O density bond had a pressure after deposition around 10^{-7} mbar (Table 3.1). Therefore, we achieved to diminish the oxygen concentration in the samples by reducing the humidity attached to the walls within the chamber after using the external heaters.

The effect of diminishing the oxygen seen in FTIR measurement was also seen in the mass spectrometer (Figure 4.1.4). The bar graph shows the different ion currents from the chamber gases. Among the gases evaluated are water, oxygen, nitrogen and hydrogen gases. A decrease in the current intensity of water and oxygen gases is observed through pressure reduction. This current intensity is proportional to gases quantities detected.

The inset shows the relative percent of oxygen. These values have been normalized with respect to neon gas due to its stability. Its behavior is similar to the Si-O bond density seen in FTIR measurement (Figure 4.1.3).

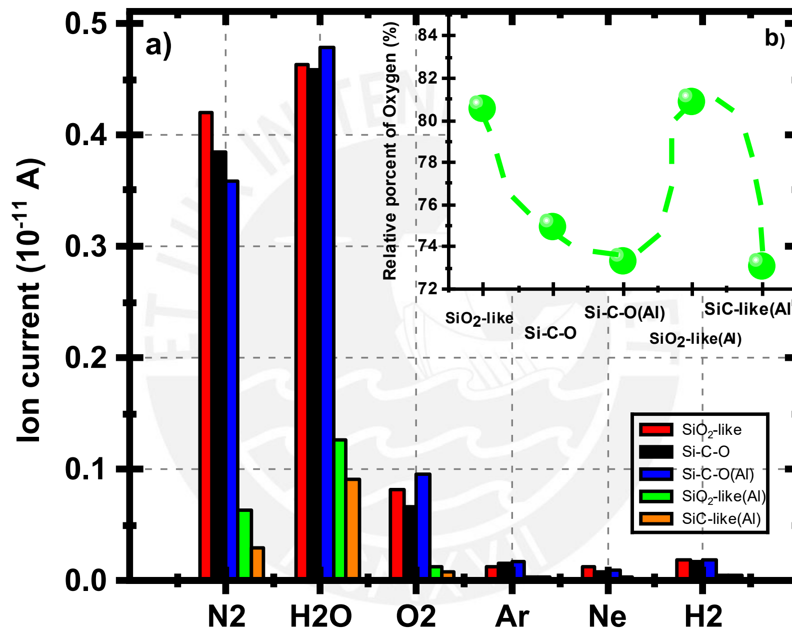

Figure 4.1.4 Bar graph portrayal of the ion current detected by mass spectrometer. Argon and Neon gases present in the air are presented in the chamber prior to deposition (a). Relative percent of oxygen versus samples deposited through of time (b).

After the installation of heaters external to the chamber, samples with low oxygen content were obtained as confirmed by FTIR spectrometry and mass spectrometry.

After having obtained the SiC-like sample with low content oxygen. The sample is characterized by structural, optical and electrical measurements. The results of the as-grown film will be presented first, followed by the results of the rapid thermal annealed sample.

4.2 Infrared spectroscopy analysis

The position, full width half maximum (FWHM) and area of the absorption band give important information about bonding characteristics and chemical structure of the film. Changes in the bonding density and peaks position enable us to study the effects of annealing. In this section, we develop the IR absorption spectroscopy analysis of the Al-doped hydrogenated SiC thin films named "*a*-SiC:H(Al)" versus the annealing treatments. In particular, the evolution of the distinct hydrogen-related bonds is assessed versus the annealing temperature and the variation of the FWHM of the Si-C bonds related to the absorption band is probed versus the annealing temperature in Rapid Thermal Annealing processes (RTP).

The infrared spectrum of the SiC-like (Al) sample is shown in Figure 4.2.1 This spectrum shows the characteristic modes of vibration *a*-SiC:H(Al), i.e. the Si-C stretching mode at 780 cm^{-1}, C-H_n wagging mode at 998 cm^{-1}, Si-O stretching mode 1100 cm^{-1}, at Si-H_n stretching mode at 2122 cm^{-1} and C-H stretching mode at about 2873 cm^{-1}. A decrease of Si- O stretching mode was observed as it was mentioned in the prior section. The most dominant mode of vibration is the Si-C stretching. This indicates the dominant role of this bond in the structure of the film. The absorption band is indicative of the amorphous nature of the silicon carbide films. The C-H vibrational modes are too small to be easily identified but it does not imply that there are few C-H bonds. This is due to its weak oscillator strength, which is further weakened by three-quarters of Si-C bonds [15]. This is consistent with the fact that the electronegativity difference is larger for Si-H bond than the Si- H bond length [62].

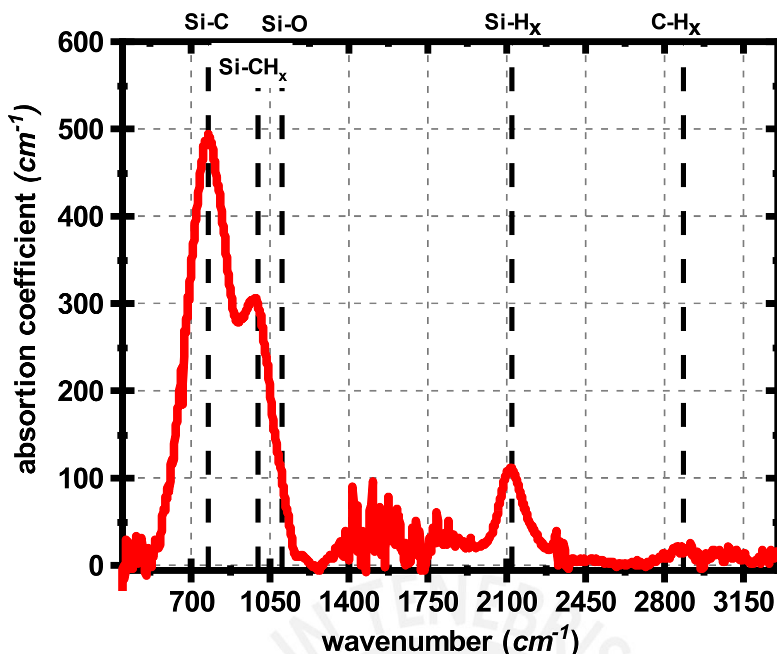

Figure 4.2.1 IR absorption spectrum over 400 cm^{-1} – 3300 cm^{-1} of *a*-SiC:H(Al) before any thermal treatments. Different are identified and labeled here. It is important to recall that this sample was the one that presented the lowest oxygen amount. This is in an almost no observable shoulder around ~1100 cm^{-1}.

The SiC-like (Al) sample was subjected to rapid thermal annealing (RTA). The RTA was carried out at 200 °C, 300 °C, 400 °C, 600 °C for 600 seconds. Changes on the film were observed after annealing treatment.

The IR absorption spectra after annealing at distinct temperatures is shown in Figure 4.2.2. For comparison, the spectrum of the as-grown (AG) film is also shown. All spectra exhibit three main bands. These spectra show mainly the presence of a broad absorption band in the region 500-1300 cm^{-1} and two less-intense bands located in the 2000-2200 cm^{-1} and 2800-3100 cm^{-1}. The peaks are identified as follows:

a) The different modes of vibration are respectively centered at 440 cm^{-1} for Si-O-C rocking, at 520 cm^{-1} for Si-Si stretching mode, at 615 cm^{-1} associated with a bonding between Al and either Si or C. Finally a weak band around 530 cm^{-1} resulting from C- H bond [16][63].

b) The band centered at 780 cm^{-1} is attributed to the Si-C stretching vibration mode. The band width is broadened due to the angular distortion of Si-C bonds in the amorphous structure of the thin film [56].

c) The shoulder around 1000 cm^{-1} is assigned to the wagging vibration of CH_2 or CH_3 groups attached to silicon atoms. These bonds may result from the higher bonding preference of carbon for hydrogen [61]. Furthermore, sub-stoichiometric SiO_x ($x<2$) structural fragments are known to present a broad absorption band at around 1100 cm^{-1} [44].This band is actually composed of four bands from which only an average resulting in two peaks at 1065 cm^{-1} and 1190 cm^{-1} are resolved [58].

d) The absorption band between 2000 cm^{-1} and 2200 cm^{-1} correspond to the stretching vibration of Si-H_n bonds. For solely a-Si:H, the mode of vibration is 2000 cm^{-1}. This mode shifts to a higher wavenumber due to a network bonding configuration in the case of a-SiC:H [45].

e) The band peak from 2800 cm^{-1} to 3000 cm^{-1} is associated to the C-H_x stretching mode. The peak 2890 cm^{-1} and 2960 cm^{-1} correspond to stretching mode C-H_2 and C-H_3, respectively. Its signal is weak due to a reduced oscillator strength [4].

An increase in the intensity can be seen in the absorption band attributed to Si-C stretching mode with annealing temperature at 600 °C along with a slight shift of to lower wavenumber. Also, the intensities of the absorption bands around 2100 cm^{-1} and 2800 cm^{-1} are reduced with annealing after 400 °C.

In order to find how the bond density, change after annealing, a deconvolution of the band in the spectral region 500-3300 cm^{-1} were made with Gaussians curves. The deconvolution of the band in the spectral region 500-1100 cm^{-1} is shown in Figure 4.2.3, whereas that band in the region 1500-3300 cm^{-1} is shown in the inset. These were performed after each annealing treatment.

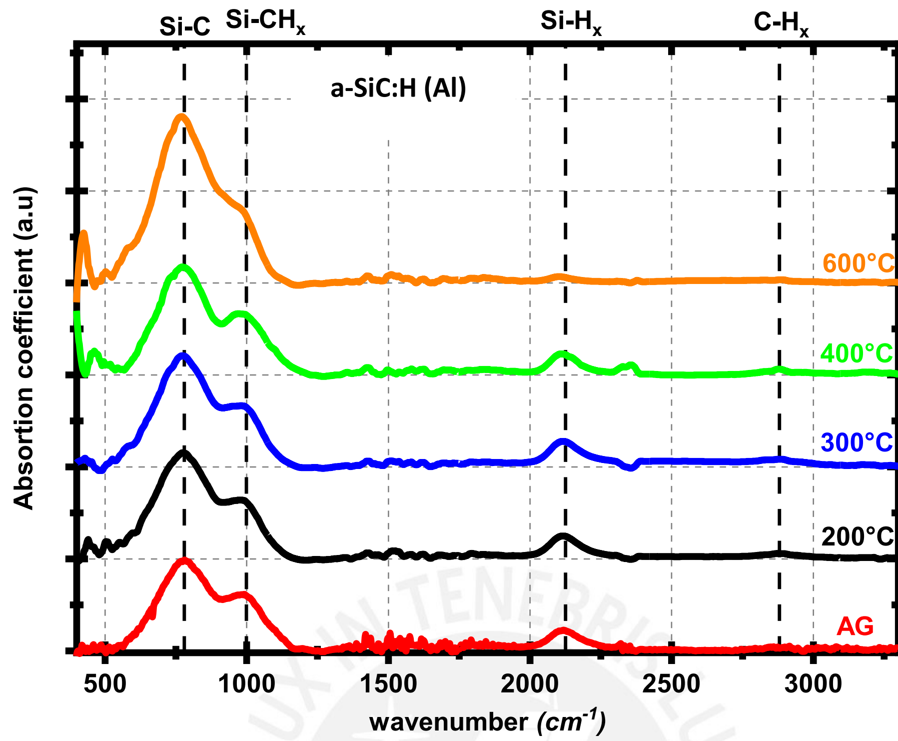

Figure 4.2.2 IR absorption spectra over 400 cm^{-1} – 3300 cm^{-1} of sample the *a*-SiC:H(Al) at after different annealing temperature. AG stands for as grown. Different bonds are identified and labeled.

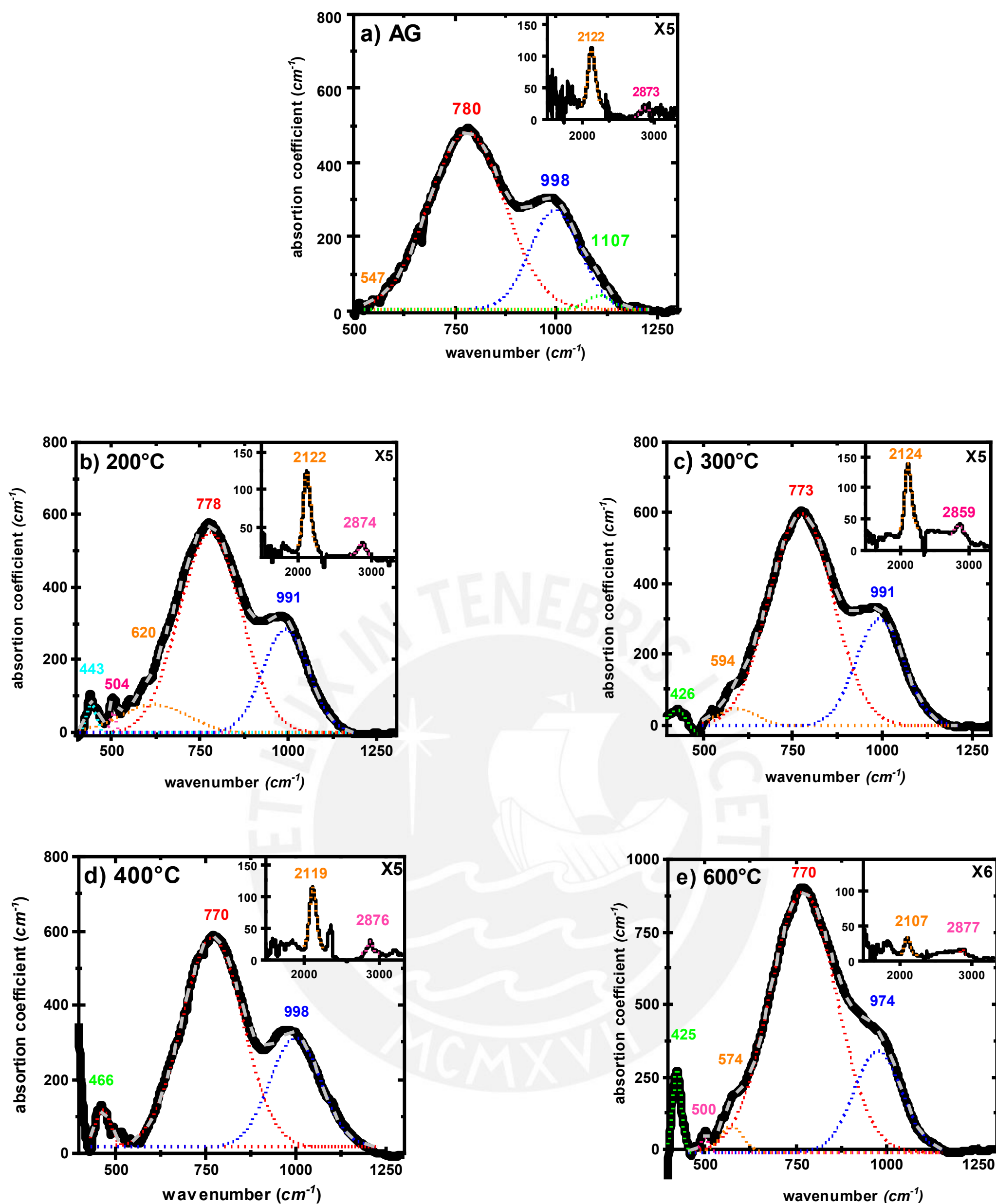

Figure 4.2.3 Deconvolutions of the IR spectra of sample at different annealing temperature in the region 400-1300 $cm^{-1.}$ Inset is the deconvolution in the region 1500-3300 cm^{-1}. Theoretical envelopes (sum of deconvoluted bands) are given by grey dash. The experimental curve is given by thick black line.

The bond densities of each vibration mode were calculated using equation 2.5.1. The bonds densities of each vibrational mode under annealing temperature are depicted in Figure 4.2.4 (a). The latter shows that there is a variation of these bond densities after annealing from 400 °C to 600 °C. The C- H bond density exhibited a noticeable decrease after annealing in the range of 300 °C to 600 °C. The behavior of the Si-H bond density below 400 °C was similar to the trend in the C-H case. As for the Si-C bond density, it started to increase after annealing at 300 °C and exhibit a linear increase with increasing temperatures. After 400 °C, the hydrogen-related bonds almost vanished, as a consequence of the out-diffusion of hydrogen from the sample. This observed effect is quite similar to that observed in a-SiC:H films deposited by magnetron sputtering technique, reported in detail in Refs [6][64]. Furthermore, the decrease in hydrogen bonds is related also with a shift to lower wavenumber of the Si-H bond as shown in Figure 4.2.4 (b). This shift is due to changes in local electronic environments of Si, C, H, likely due to thin film densification, which can be due to a possible change of the Si-H bond configuration. Back bonding of other atoms to the silicon atom modifies its vibration mode due to changes in electronegativity [45].

The fits for the Si-C bonds in the FTIR spectra were Gaussians, reflecting the nature random distribution of the bonding configuration of the amorphous state. The variation of the full-width half maximum (FWHM) of these peaks reflects the variation on this random distribution of bonding configuration. Figure 4.2.5 (a) depicts the changes in FWHM versus the annealing temperature. The $C\text{-}H_x$ bond attached to silicon atoms is still present after annealing.

The formation of new Si-C bonds is a consequent of the breaking of $Si\text{-}H_n$ and C-H bonds. The present of $Si\text{-}CH_x$ bond is likely due to the breaking of $C\text{-}H_3$ bonds to form new $C\text{-}H_2$ bonds due to the interaction of hydrogen with carbon dangling bonds and/or unsaturated C=C bonds [64].

Hydrogen content was calculated from FTIR following the previously published reports [42][44][79]. The amount of hydrogen can be calculated directly the number density of hydrogen-related bonds as the sum of Si-H and C-H bonds. This is plotted in Figure 4.2.5 (b). The slight increase of hydrogen content in the lower temperature range corresponds likely due to a reduction of voids in the sample [65]. At a temperature higher than 400 °C, the hydrogen content decreases, suggesting the out-diffusion of all hydrogen-related molecules. As hydrogen effuses, a transformation of the structure takes place.

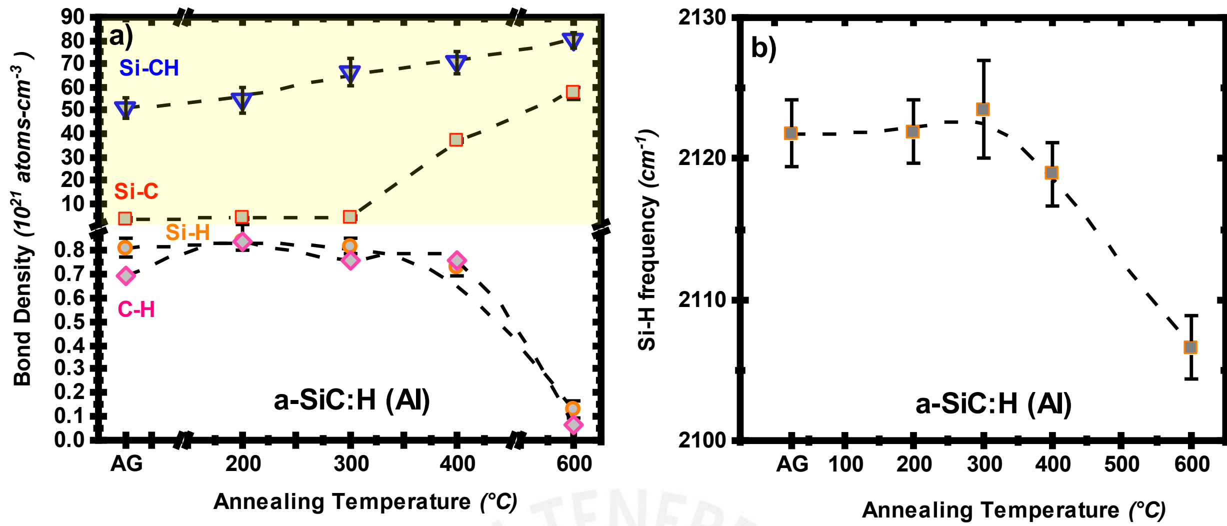

Figure 4.2.4 Bond density of Si-C, Si-CH, Si-H and C-H bonds as a function of annealing temperature for the *a*- SiC: H(Al) (a). Peak position of Si-H stretching mode as a function of annealing temperature (b).

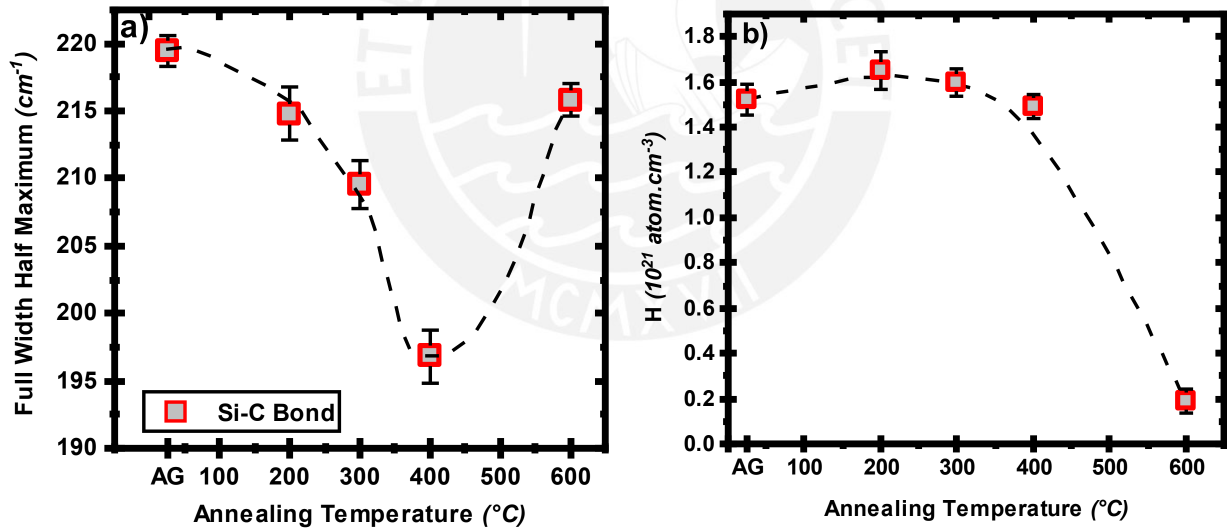

Figure 4.2.5 Full Width Half Maximum of the Gaussian fit on Si-C bands versus annealing temperature (a). Evolution of the Hydrogen content versus annealing temperature (b). Dashed lines are a guide to the eye.

4.3 XRD patterns

XRD measurements were carried out to investigate the thin film structure prior to and after annealing.

Fig 4.3 shows the XRD patterns (without background correction) of a-SiC:H(Al) films as-grown and after annealing at 600 °C. Both samples show a broad diffraction peak at around $2\theta = 14\,°$, which correspond to the amorphous structure of the sample holder that it was not eliminated in the data collection. A similar report can be found in Ref [66]. In addition, a broad diffraction peak around $2\theta = 28°$, reveals that the deposited films are a dominantly amorphous state [67].

In particular, the inset of Figure 4.3 shows the magnified XRD pattern (As grown) in order to see the formed phase of aluminosilicate, which is the superposition of alunite and quartz. Green sharp diffraction peak ($2\theta = 20\,°$ and 26 °) are related to quartz while that purple sharp diffraction peak ($2\theta = 25\,°$) is related to alunite [68]. It shows the presence of aluminum in our sample, as expected. On the other hands, the absence of these diffraction peaks on the XRD pattern after 600 °C suggests that aluminum atoms have new bonded on the SiC matrix of the sample.

The presence of aluminum atoms was observed, this is also seen in the SEM-EDS measurement. The amorphous structure was verified prior to and after rapid thermal annealing.

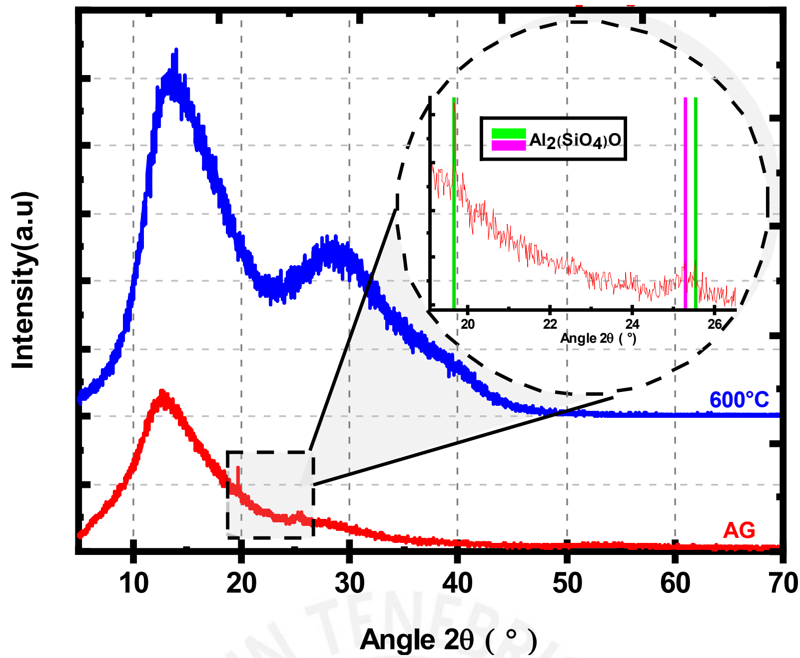

Figure 4.3 XRD patterns (without background correction) of an as-grown sample of *a*-SiC:H(Al) and after annealing at 600°C. The spectra are vertically displaced for the sake of clarity. The inset show magnified XRD pattern in the range of 2θ between 19 ° - 27 °.

4.4 Raman spectroscopy analysis

The IR spectra of *a*-SiC:H(Al) provide information on the asymmetrical bonds such as Si- H, C- H, Si-C, etc. The absorption bands due to Si-Si and C-C bonds cannot be detected by IR measurements as they are infrared inactive.

Raman scattering spectra in the range of 100 -1800 cm^{-1} for the *a*-SiC:H(Al) thin film in as-grown and at 600 °C is shown in Figure 4.4.1. The spectra exhibit three regions, which are assigned to Si-Si (100-600 cm^{-1}), Si-C (650-1050 cm^{-1}) and C-C (1250-1650 cm^{-1}) vibrational modes. This result is in good agreement with the previously reported by Melinon *et al* [1]. The main vibration modes are given by:

a) It can be observed that the sample of the as-grown and after 600 °C annealing exhibit a typical signature of c-Si with Raman shark peak position at around 521 cm^{-1} [69]. This is a contribution of the c-Si substrate due to a large penetration depth of the Argon laser source that operating at 514.5 nm. Typical

penetration depth is about 500 nm, which exceed the thickness of the film as is reported by Compagnini *et al* [70].

b) The broad peaks centered at 170 cm^{-1} and a shoulder on the low wavenumber side of c-Si the 473 cm^{-1} are assigned to the Si-Si transverse acoustic (TO) and transverse optical (TA) vibration mode in amorphous configuration respectively [15][71].

c) The absorption band at 660, 760, 780, 950 and 960 cm^{-1} is attributed to Si-H (wagging/bending), amorphous Si-C, transverse optical (TO) and Longitudinal optical (LO) modes of 3C-SiC and second order of transverse optical (TO) mode of Si-Si vibrations, respectively [72][73].

d) The band centered at around 1450 cm^{-1} is composed of two bands at 1360 cm^{-1} and 1575 cm^{-1}, corresponding to graphite (sp^2) and diamond (sp^3), respectively [74].

It can see that the Raman spectra of the as-grown (AG) and annealed at 600 °C show the above-mentioned peaks and that is related to the amorphous nature of the material. In order to obtain the position of the main vibration's modes and full-width half maximum a deconvolution was made on the spectra as it is shown in Figure 4.4.2.

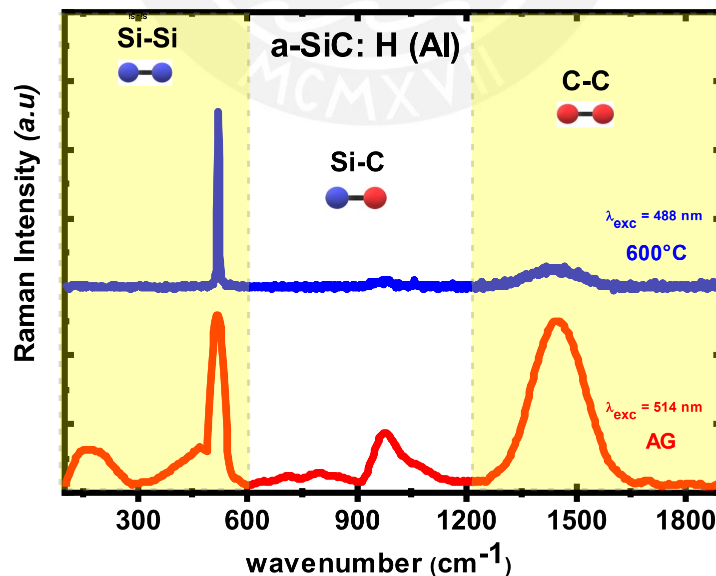

Figure 4.4.1 Raman spectra of an as-grown sample of *a*-SiC:H(Al) and after annealing at 600 °C. Different bonds are identified and labeled here. Excitation source was changed to reduce the

exposition of the substrate to the incoming radiation (Raman measurement). The spectra are vertically displaced for the sake of clarity.

For the 100-600 cm^{-1} spectral region of the as-grown sample, the best deconvolution of the band shows the presence of a peak centered respectively at 167 cm^{-1} and a broad peak centered at 468 cm^{-1} characteristics of a predominant amorphous structure. Whilst at 600 °C there is a phase change by the absence of the peaks due to amorphous Si- Si, only show a peak around at 520 cm^{-1}. It is due to that the band centered around 468 cm^{-1} that shifts to 520 cm^{-1} and become much narrow suggesting the formation of microcrystalline silicon as is reported by Neto *et al* [59]. Even if this could be evidence of silicon crystallization, X-ray diffraction analysis after annealing at 600 °C as is mentioned in the prior section, it did not reveal any indication of silicon crystals in the films. Thus, the observed behavior could be in fact due to a reduction of thickness as a consequence of hydrogen release and band gap increase, it is due to the exposition of the substrate to the incoming radiation during Raman measurement. For the latter, reason the measurement of the annealed sample was performed under 488 nm excitation in order to reduce the mentioned effect.

For the 600-1200 cm^{-1} spectra region to as-grown, the deconvolution of the bands shows the presence of the absorption band at 640 cm^{-1} is attributed to Si-H. Furthermore, this spectrum reveals the peak centered at 786 cm^{-1} that correspond to amorphous Si-C. The absorption band at 973 cm^{-1} is attributed to transverse optical mode vibration of Si-C [71]. After 600 °C annealing the absorption band at 640 cm^{-1} not appears and the absorption band at 973 cm^{-1} remains. This could be attributed to Si clusters with a small quantity of SiC particles [75].

For the 1200 -1600 cm^{-1} spectra region at as-grown, the deconvolution of the bands shows the presence of the peak centered at 1450 cm^{-1} is related to two peaks that correspond to graphite and diamond. Upon annealing up to 600 °C a displacement of this peak to a lower wavenumber is indicative of a graphitization process forming large sp^2 carbon islands. The graphitization and hydrogen evolution are closely related to each other [59].

This is also been shown in the FTIR analysis with the increase of Si-CH_2 and Si-C bond density due to depletion of C-H_3 (sp^3 carbon).

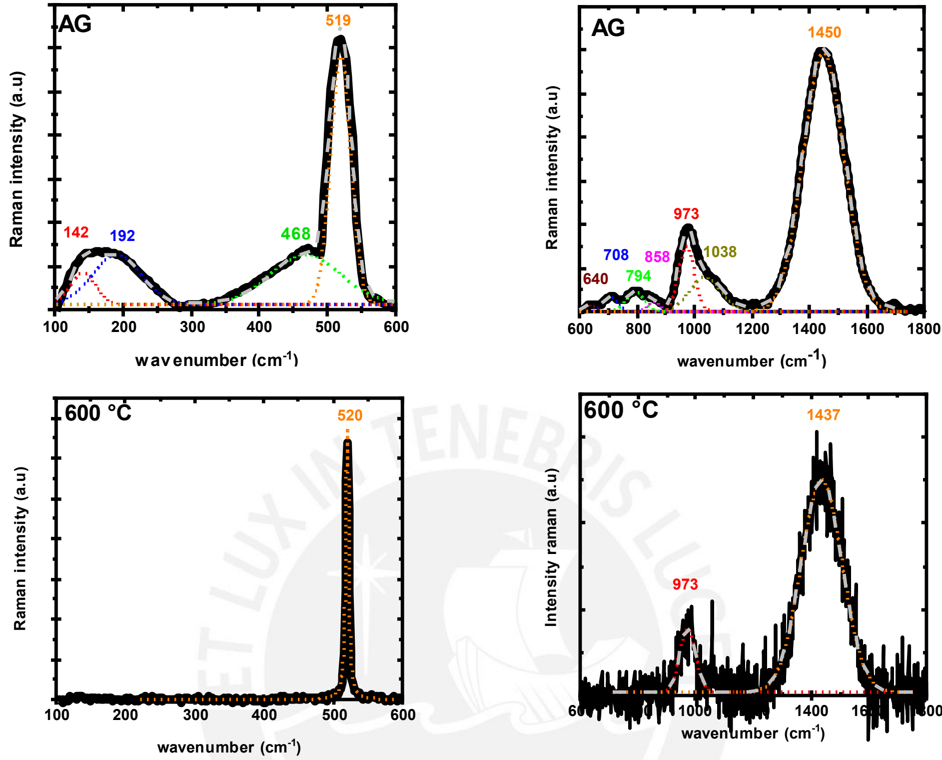

Figure 4.4.2 Deconvoluted of the Raman spectra of as grown and annealed at 600 °C in the region 100-1800 cm^{-1}. Theoretical envelopes (sum of deconvoluted bands) are given by grey dash. The experimental curve is given by thick black line. AG stands for as grown.

4.5 Optical characterization and analysis

UV/VIS/NIR spectral transmittance measurement was performed in order to determinate the optical properties and optical energy band gap of the *a*-SiC:H(Al) samples. A variation of the Swanepoel method was used [28][31]to determine the refractive index, thickness and absorption coefficient are obtained the films. From the absorption coefficient, it is possible to calculate the optical energy band gap values and asses its dependence with thermal annealing treatments.

Figure 4.5.1(a) shows the transmittance spectrum of the *a*-SiC:H(Al) film deposited of as-grown and after treatments at high temperatures. These spectra can be divided into three regions.

Transparent, medium-weak and strong absorption. Transmittance spectrum depends on the refractive index, extinction coefficient, absorption coefficient, thickness and wavelength. The transmittances presented here exhibited similar oscillations from a sample without annealing and annealed up to 400 °C due to a similar thickness. While after 600 °C, it shows a shift to lower wavelength due to a change in thickness and refractive index.

It is observed that to low annealing temperatures the thickness remains constant. Whilst at annealing temperatures higher than 400 °C, the thickness shows a remarkable decrease, so-called densification, due to crystallization. Thickness decreases from 321 nm to 266 nm. The origin of this change is likely due to local changes associated with structural relaxation. Furthermore, its reduction is related to an increase of mass density, approaching to the mass density of c-SiC [56]. For comparison with other investigations [14][76], relative volume was a plot against annealing temperature as shown in Figure 4.5.1 (b).

The refractive index is another optical parameter that is related to local changes and densification of the film upon annealing temperature. The effect of rapid thermal annealing (RTP) is shown in Figure 4.5.2. It shows that the refractive index (n) increases with annealing temperature. For instance, at a wavelength of 800 nm, an increase from 2.11 to 2.16 nm our sample is observed. For comparison, the refractive index of SiO_2-like, SiCO-like, SiC-like matrix is shown. The refractive index of our samples is in the range between SiCO and SiC. We attribute the increase of the refractive index to densification processes related to the hydrogen evolution from the film. Friessnegg *et al.* reported also an increase of the refractive index of a-SiC:H sample due to densification for above about 500 °C by RTP [19].

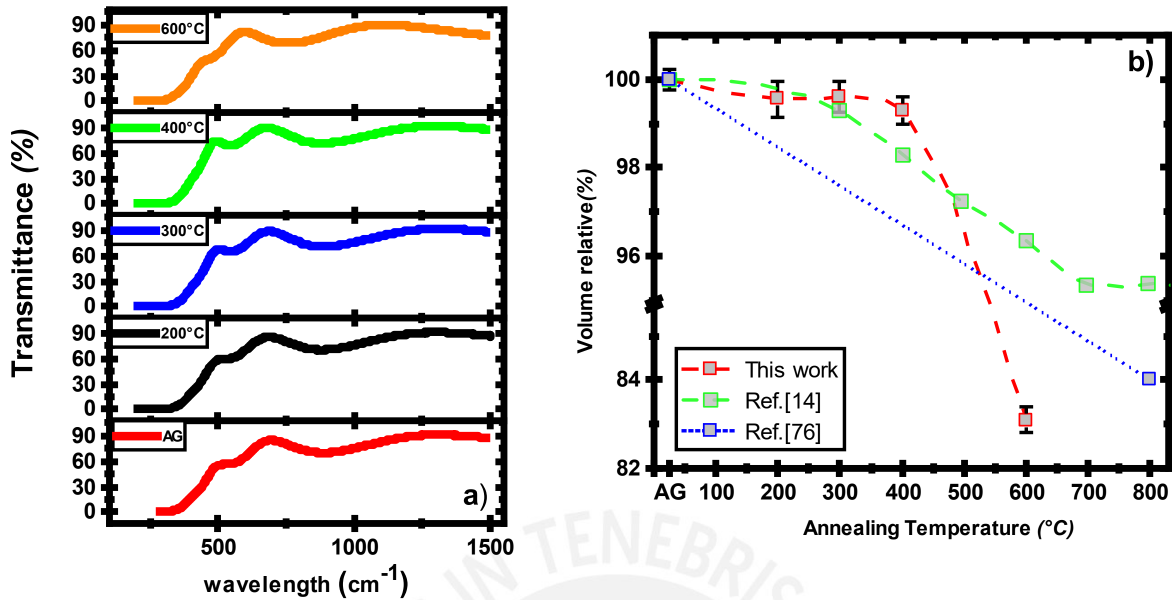

Figure 4.5.1 Transmittance spectrum over 190 cm^{-1} – 1500 cm^{-1} of sample *a*-SiC:H(Al) grown on fused silica at different annealing temperature (a). Volume relative change of annealed to as-grown one. Green, blue and red square represent the relative volume from [14][76] and this work. The line is drawn to provide guidance to the eye (b).

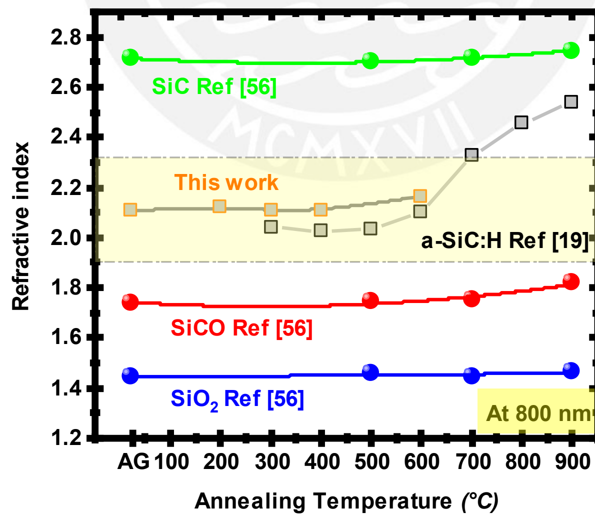

Figure 4.5.2. Refractive index at 800 nm wavelength of *a*-SiC:H(Al) from As-grown to 600 °C. Data obtained in this work is plotted alongside the refractive index of SiO_2, SiCO, SiC:H, SiC from the indicated references.

Then, from the absorption coefficient and different models is possible to extract the optical energy band-gap. Currently, there are a different approach to estimate the band gap of an amorphous material. In this work was used Tauc energy, isoabsorption energy E_{04} and band fluctuations model from which the Urbach energy is obtained also.

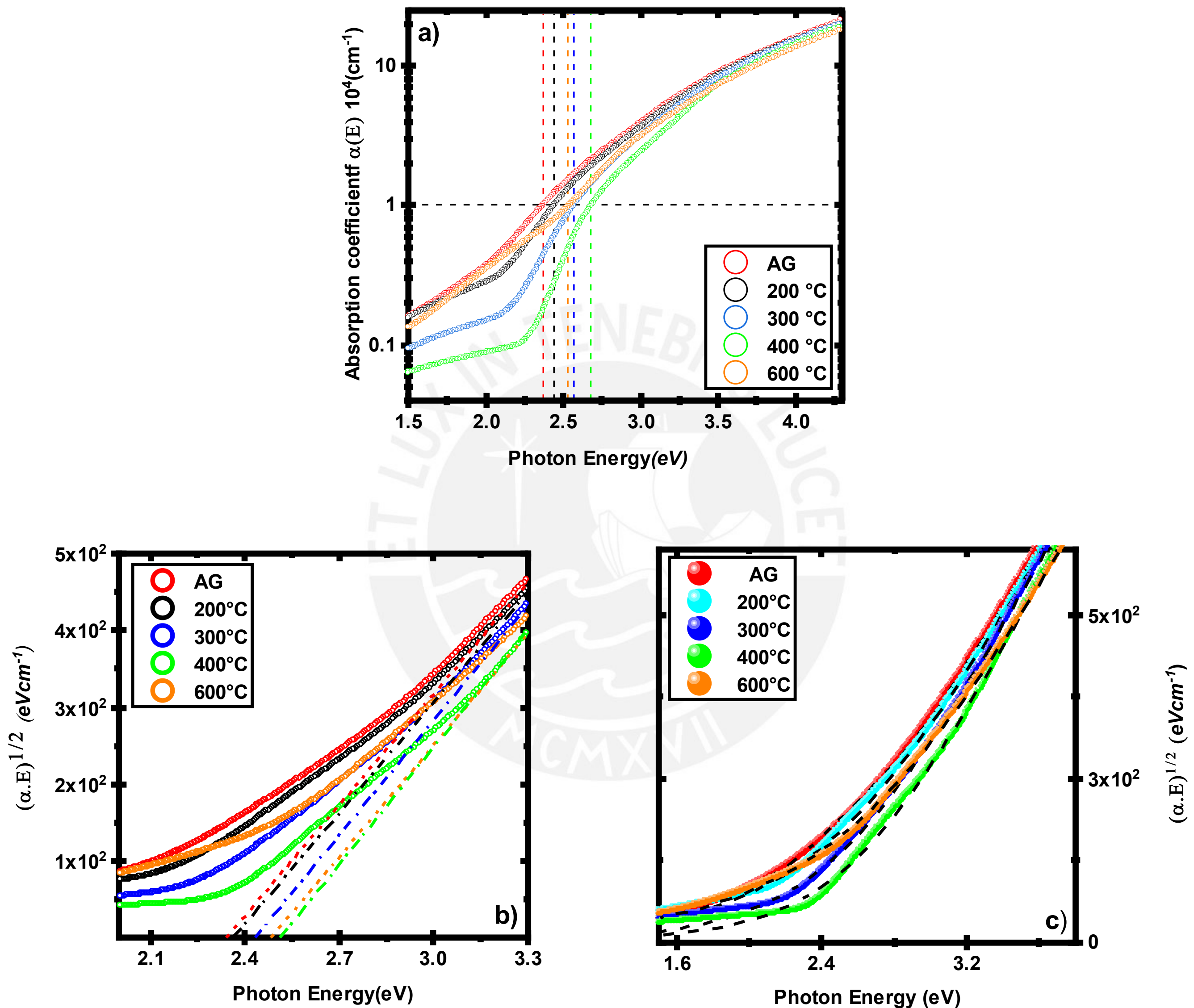

Figure 4.5.3. Absorption coefficient in logarithm scale along with the E_{04} energy value (a). Tauc-plot showing a good linear behaviour the high energy region (b).

To determine the energy bandgap values by isoabsorption energy, The E_{04} value is defined as the energy at which the absorption coefficient is equal to 10^4 cm^{-1}, see Figure 4.5.4 (a). While to determine by model Tauc, we plotted $(\alpha h\nu)^{1/2}$ versus $(h\nu)$ where α is the absorption coefficient and $h\nu$ is the photon energy and performing a linear fit of the fundamental absorption region, as shown in Figure 4.3.3 (b). The intercept of the linear fit with the energy axis is the Tauc-gap [6][31]. Notice the good linear relationship of the absorption coefficient in the Tauc-plot representation. Furthermore, to retrieved the values of energy band gap by band-fluctuations model, also we plotted $(\alpha h\nu)^{1/2}$ versus $(h\nu)$. Where performing a fit that merges of Urbach and absorption edge regions in a single equation as depicted in Figure 4.5.3 (c).

Figure 4.5.4 (a) shows the band-gap presents a similar dependency with annealing temperature independently of the model used for its calculation. Furthermore, it shows that the E_{04} iso-absorption gap values are greater than Tauc gap values. This finding is consistent with the result observed for another structural disorder system such as a-C:H [29]. This behaviour can be attributed to that the Tauc gap is associated with optical transitions between extended states close to the band edge, while the E_{04} gap corresponds to transitions of those extended states well beyond the band edge [29]. The decreases of the band-gap with increased annealing temperature seem to correlate well with the loss of hydrogen in the film. Since Hydrogen plays an important role in the electronic structure and optical properties of the hydrogenated amorphous semiconductor, this effusion of hydrogen upon annealing would likely lead to a population of dangling bonds and defect state, which in turn result in an enhanced density of highly localized sates below the mobility edge, thereby decreasing the optical gap. Whilst, values of optical bang gap determinate by band-fluctuation model have a different behaviour against annealing temperature. It is observed that the band-gap increases with the annealing temperature. This behaviour is expected due to that with the annealing the film suffers a shrinking of thickness, at annealing which is consistent with the previous result in Figure 4.5.1(b), thus entailing a reduction of the mean lattice constant and independently of thermal-induced hydrogen out-diffusion or even for non-hydrogen samples [6].

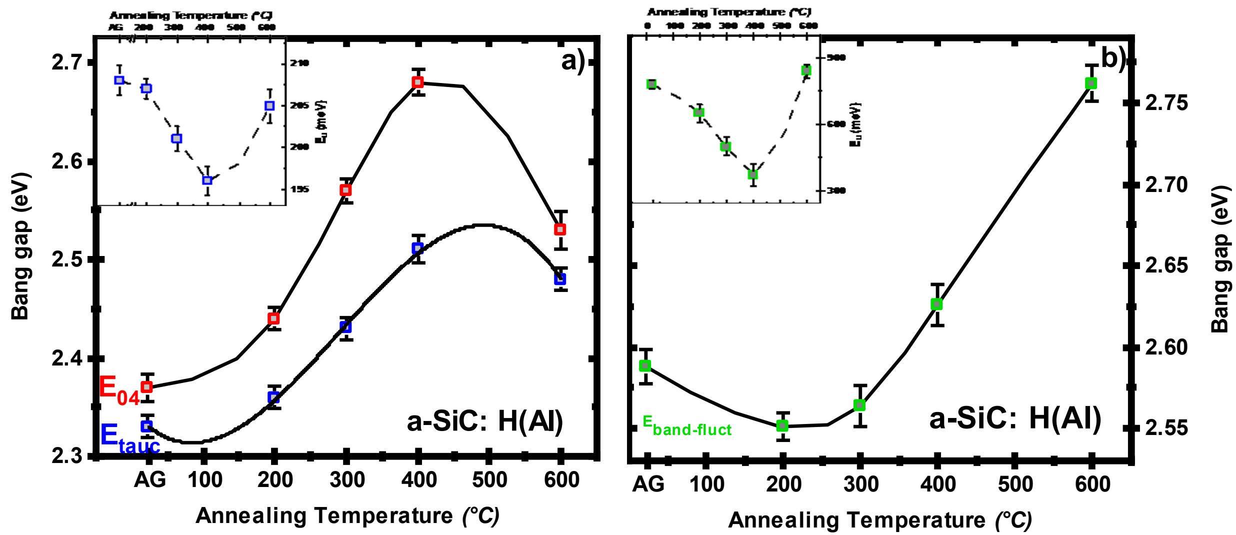

Figure 4.5.4 Energy values (E_{Tauc} and E_{04}) of a-SiC:H(Al) after annealing temperature (a). Inset (a) shows change of the Urbach-slope with the annealing treatment. Energy values using band-fluctuations model of a-SiC:H(Al) after annealing temperature (b). Inset (b) shows change Urbach energy with annealing treatment using band-fluctuations model.

The Urbach energies values are determinate through of Urbach rule and band-fluctuation model. By Urbach rule, energies were obtained by performing a fit in logarithm scale of the absorption coefficient. It draws a linear equation in a linear region, where β is the Urbach slope, the inverse of Urbach energy $E_U = 1/\beta$. The band fluctuation model, the single equation below fundamental region, an asymptotic analysis leads to an exponential behavior equivalent to the Urbach rule. As it is well known, this parameter is attributed to structural disorder [25]. The inset of Figure 4.3.4 (a) and 4.3.4 (b) exhibit the same behaviour. It shows that the Urbach energy is decreasing at annealing temperatures up to 400 °C. However, upon to 400 °C annealing temperature, it increases again. The reduction could be related to structural relaxation (reduction of a topological disorder) this implies a reduction of tails states in the band edges. At more than 400 °C annealing temperature, the Urbach energy increases likely due to the effusion of hydrogen, this leads to an increase of structural disorder because of stress or shrinking of film, so that structure rearrangements occur. This result is similar to that obtained in [77][14]. Nevertheless, Guerra *et al* reported that the variation of Urbach energy is independently on the hydrogen amount after annealing treatment. This behaviour was observed also in the non-hydrogenated sample of amorphous silicon carbide [6].

The disorder of the *a*-SiC:H(Al) sample studied here is reduced with the annealing treatments (RTP) until a critical temperature, then an increase is shown. This effect has been measured by the Urbach energy and the average FWHM of the absorption peaks observed in the IR absorbance spectra as was seen in Figure 4.2.5 (a). Figure 4.5.5 shows that both measurements present the same behavior.

On the other hand, it is observed that the values energy band-gap determined by the mean of the band-fluctuations model is greater than the obtained by Tauc model and E_{04} isoabsorption. This is due to the fact that Tauc-energy and the E_{04} iso-absorption gap are subjected to the spectral region overlapped by the Urbach tails. This can be seen in the inverted behaviour of the Urbach energy and energy optical bandgap shown in Figure 4.5.4.

The main advantage of the latter model is that no discrimination must be done between the Urbach and absorption edge region, that is, the mixing region is also part of the adjustment input. Consequently, the band-gap obtained by the band-fluctuations model is not correlated to the Urbach energy. Note that Figure 4.3.5 has a contrary behaviour to the Tauc-gap (Figure 4.3.4) [33].

Finally, the bandgap energy values used in this work are extracted by the band-fluctuations models, due to the fact that accurately describes both the Urbach tail and absorption edge regions in a single equation with only three fitting parameters. Whilst Tauc-energy and E_{04} iso-absorption take into account the superposition of the Urbach region. In particular, in amorphous semiconductors, this overlap is large due to the broadness of Urbach tails on the fundamental region.

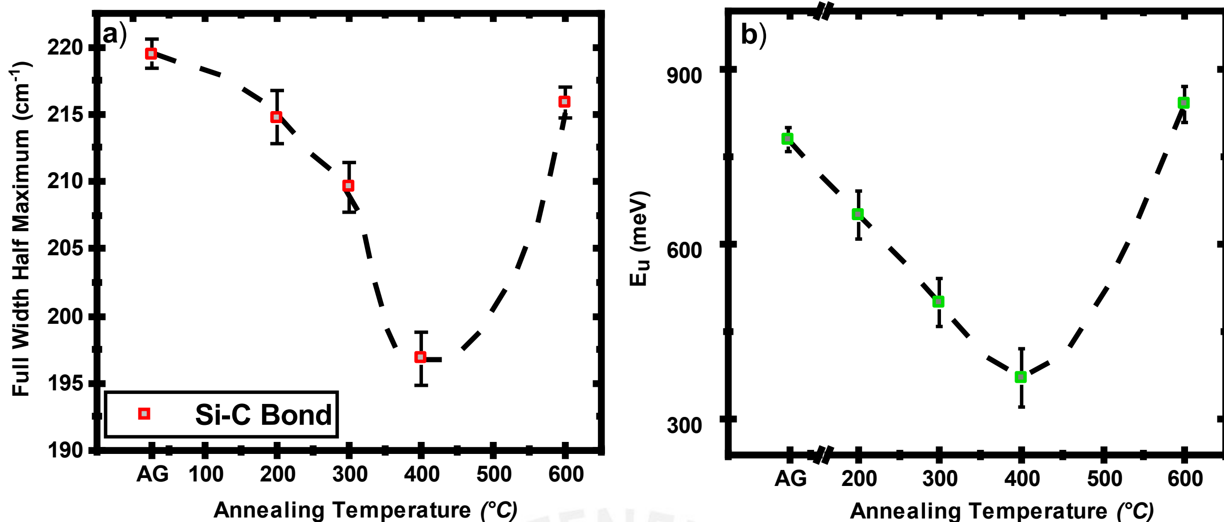

Figure 4.5.5 Full Width Half Maximum of curve gaussian fitted on Si-C mode vibrational as a function annealing temperature. The line is drawn to provide guidance to the eye (a). Urbach energy against annealing temperature by Band-fluctuations model (b) and by Urbach rule (inset b).

4.6 Electrical properties

Characterization of the *a*-SiC:H(Al) would not be complete without an evaluation of its electrical properties. In this section, the current-voltage (I-V) curves will be presented first. Then the electrical characterization was performed by the Van Der Pauw method in order to determinate conductivity values.

Contact characterization after annealing

In order to characterize contacts, I-V measurements were performed varying the current from -0.1 mA to 0.1 mA following the sequence of the contacts near the ends of the sample as shown in Figure 3.4 (b) and measuring the voltage response. Figure 4.3.6 shows four I-V curves of *a*-SiC:H(Al) film deposited from as-grown to 600 °C. In addition, it shows the configuration used for each permutation. For instance, I13-V24 indicates a current that enters by the contact 1 and is collected by the contact 3 while the voltage response is measured through contacts 2 and 4.

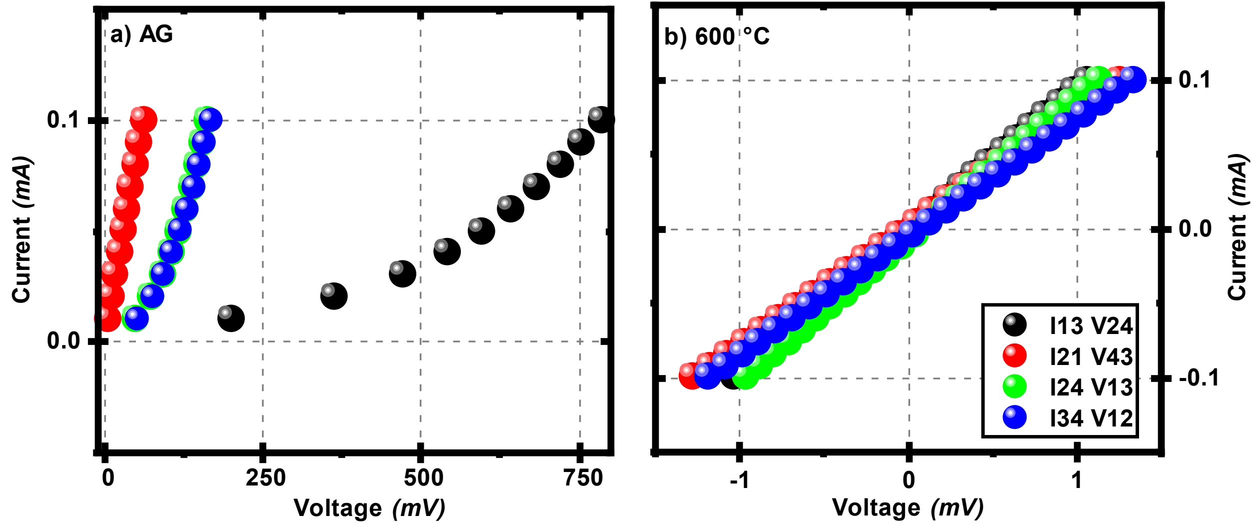

Figure 4.6.1 I-V curves over -0.1 mA to 0.1 mA of *a*-SiC:H(Al) before and after thermal treatments. Schottky behaviour is shows in the sample not heated (a). Ohmic contact is shows at 600 °C annealed (b). It is important to recall that the sample annealed at different temperature were performed I-V measurement, but the other curves not shown here as that presented Schottky behavior like at AG.

I-V curves for "As grown", 200 °C, 300 °C and 400 °C shows Schottky behaviour. Whereas at 600 °C is observed Ohmic contacts, due to its linear tendency. The resistance for each contact is obtained with the slope of the I-V curve. It observed that after temperature annealing, the contacts resistance is reduced. This tells us that the aluminium penetrates the film surface and facilitates a certain amount of beneficial Al / *a*-SiC:H(Al) interdiffusion due to the decrease of potential barrier that exist between aluminum and film, which depends critically on the temperature above 350 °C [78] and likely a doping near the interface p^+ produces a deflection zone very thin. The mechanism of conduction that dominates is tunnelization.

In order to determine the conductivity value by means of the Van Der Pauw method, certain conditions mentioned in chapter 2 should be met. Ohmic contact values were obtained at 600 °C and the resistance values for each permutation are shown in Table 4.6.1. Similar values of the resistances indicate the homogeneity of the sample, one of the conditions for using Van Der Pauw equation.

Table 4.6.1 The resistance values for each permutation of the sample a-SiC:H(Al)

Resistance	$R_{13\text{-}24}(10^5\Omega)$	$R_{21\text{-}43}(10^6\Omega)$	$R_{24\text{-}13}(10^5\Omega)$	$R_{34\text{-}12}(10^6\Omega)$
a-SiC: H(Al) at 600°C	(10.50 ± 1.07)	(12.65 ± 2.39)	(10.50 ± 1.16)	(12.65 ± 2.16)

Finally, the characteristic resistance values (R_a and R_b) and thickness value are parameters for to determinate electrical resistivity and conductivity values. These values are shown in Table 4.6.2. This value is compared with the values of a-SiC:H(Al) and p-type a-Si:H that were deposited by sputtering technique [17][79][80] as it is showed in Figure 4.6.2. The effect of hydrogen incorporation on the a-SiC:H(Al) and a-Si:H(B) samples result in a decrease in electrical conductivity. This decreases of electrical conductivity in both cases are related to the passivation of accept atoms by hydrogen through the creation of Si-H-(B or Al) bonds [79]. The conductivity measured at moderately low temperature probably is due to the contribution from both hopping conductions between localized states and the hops between nearest sites. This causes a change in the slope of $\log(\sigma)\ vs\ 1000/T$ curves where the extrapolated straight-line fit gives values of electrical conductivity at higher temperature [80]. This is due to that the fact the film tends to reduce the density of localized states in the neighbourhood of the Fermi level by incorporation of hydrogen, which quenches the electrical conductivity by hopping mechanism.

The value of electrical conductivity measured at room temperature (RT) of a-SiC:H(Al) taken to treatment thermal (RTP) is within the range between $\sim 10^{-4}\ \Omega^{-1}.\text{cm}^{-1}$ and $\sim 10^{-9}\ \Omega^{-1}.\text{cm}^{-1}$. This value after annealing treatment (600 °C) is reasonable because the hydrogen content decreases with annealing, which causes the decreases of numbers of dangling bonds and the so-called voids decrease too, see section 4.2. In addition, this leads to changes in the structure itself that is related to an increase of mass density, see 4.5.1 (b). All electrical, optical and structural properties and the effect of dehydrogenation appear to be broadly consistent with other tetrahedrally coordinated amorphous semiconductors.

Table 4.6.2 The characteristic resistances, resistivity and conductivity values

	$R_a(10^5\Omega)$	$R_b(10^6\Omega)$	Thickness(nm)	$\rho\ (10^5\Omega.\text{cm})$	$\sigma\ (10^{-6}\Omega^{-1}.\text{cm}^{-1}$
a-SiC:H (Al) at 600 °C	(10.50 ± 1.07)	(12.65 ± 2.39)	(266 ± 1.3)	(1.4 ± 0.2)	(7.3 ± 0.2)

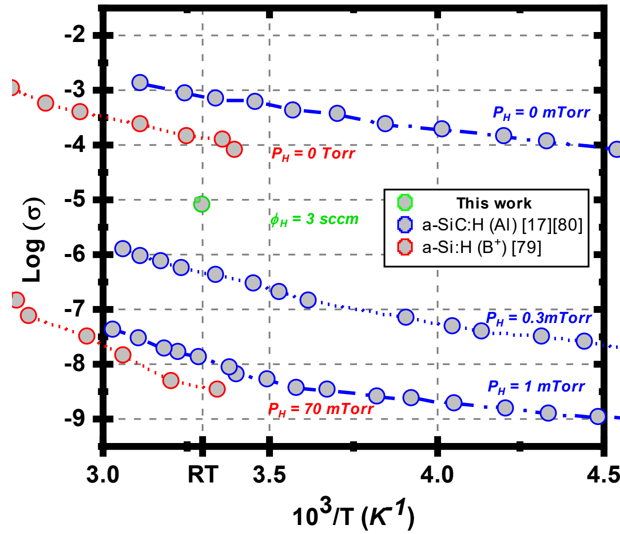

Figure 4.6.2 Plot of $\log(\sigma)$ versus $(\frac{10^3}{T})$. Electrical conductivity value of *a*-SiC:H(Al) sample at 600 °C annealing treatment (*ex-situ* measurement). Data obtained in this work is plotted along-side the *a*-SiC (Al) and *a*- Si(B^+), hydrogenated and hydrogenated from the indicated references. Here RT means room temperature.

Ellipsometry measured was performed in order to the determinate thickness of the film. It was found that the existence of an oxide layer between film and substrate with the thickness of 63 nm, as shown in Figure 4.6.2. This oxide layer was formed due to the presence of residual oxygen in the chamber prior to the start of the deposition process. It allows ensuring that the measurement of electrical conductivity is only of the film *a*-SiC:H(Al) and no from the Si substrate.

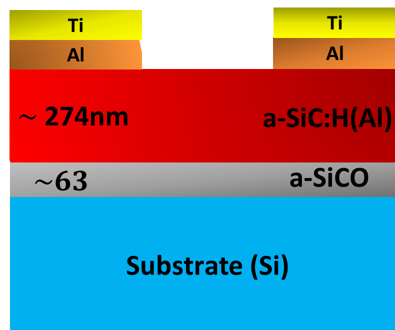

Figure 4.6.2 Structure of contact Ti-Al / *a*-SiC:H(Al) / *a*-SiCO / Silicon obtain by ellipsometry prior annealing treatment.

Conclusions

In this work, p-type *a*-SiC:H layers were grown by radiofrequency magnetron sputtering using high purity SiC and Al targets. The structural, optical and electrical properties of this amorphous wide bandgap semiconductor material with lower oxygen content have been investigated. The characterized material was also incorporated in the manufacture of a photoelectrochemical device. From this research work, the following remarks concerning the impact of rapid thermal annealing treatments are driven.

1. Structural properties

    a) SEM-EDS analysis allows the identification of the elemental composition of the film such as Silicon, Carbon, Oxygen and Aluminium. There is no detectable change in the elemental compositional of the sample prior to and after the annealing treatment. Note that the thermally induced hydrogen out-diffusion cannot be detected by EDS measurements.

    b) XRD patterns of the as-grown films revealed an amorphous state. The amorphous sample was heated at temperatures of 200 °C, 300 °C, 400 °C and 600 °C. The sample annealed at 600 °C still remained in an amorphous state.

    c) Raman scattering spectra provide information on homonuclear bonds such as Si-Si and C-C vibrational modes of the films prior to and after annealing treatments. After annealing at 600 °C changes in the C-C bonds take place. Likely, the formation of large sp^2 carbon islands indicate a graphitization process.

    d) FTIR spectra allowed the identification of heteronuclear bonds of *a*-SiC:H(Al). Si-C, Si-H, Si-O, C-H, Si-CH vibrational modes were found for samples grown using SiC and Al targets. After annealing treatments at temperatures higher than 400 °C, the hydrogen bond concentration decreased dramatically, suggesting the out-diffusion of hydrogen molecules. This desorption is related to changes in the structure [45][64][65].

2. Optical properties

    a) Optical constants of *a*-SiC:H(Al) were determined by transmittance measurements. A variation of the Swanepoel's method was used to determine thickness, refractive index and absorption coefficient. The latter coefficient was used to calculated the optical bandgap. After thermal treatments at a temperature

of 600 °C, an increase of the refractive index and a decrease of thickness are observed. This indicates the occurrence of densification processes related to the hydrogen evolution from the film, which is in accordance with FTIR results presented in this work and the literature [14][19].

b) The traditional Tauc and E_{04} iso-absorption model were used to determine the optical bandgap energy from the absorption coefficient. Both energy values presented the same behavior with the annealing treatment of the RTP. Additionally, a band-fluctuations model was used, taking into account the effects of the Urbach tails on the fundamental absorption region in a single mathematical expression. Thus, having the advantage to fit both regions simultaneously. This is in contrast to the traditional models, which require a separation of the optical absorption in these two regions.

The optical band gap energy values extracted by the band-fluctuations model increased from 2.55 eV to 2.76 eV after annealing treatments. A Possible explanation for the latter could be related to desorption of hydrogen, which results in the formation of new Si-C and C- C(sp^2) bonds. In addition, an out-effusion of hydrogen is related to the shrinking of film, which causes the reordering of the amorphous network. A shrinking of the bond length can be translated into an increase of the optical band gap [6][33].

c) The Urbach energies were calculated through the Urbach rule and the band-fluctuations model. Both models exhibit the same behaviour of the Urbach energy with the annealing temperature: a decrease of the Urbach energy is observed for temperatures of up to 400°C, followed by a subsequent increase for higher annealing temperatures [6]. This indicates that there is a thermally induced reordering of the amorphous matrix and shrinking of the mean bond length. Furthermore, the same behaviour was observed on the FWHM of the Si-C related absorption band obtained by FTIR means supporting this result.

3. Electrical properties

The electrical conductivity of Al doped-*a*-SiC:H is obtained through I-V curves by means of the Van Der Pauw method. The determination of the conductivity could only be achieved after thermal treatments at 600 °C. This due to the formation of an ohmic contact between the *a*-SiC:H(Al) and the contact material. Thermal treatments induced the diffusion of the aluminum contacts on the film, which is reflected in an Ohmic behavior of the electrical contacts.

The electrical conductivity of the film measured by Van der Pauw technique was $(7.3 \pm 0.2)\ 10^{-6}\ \Omega^{-1}.\mathrm{cm}^{-1}$and is within the range of $\sim 10^{-4}\ \Omega^{-1}.\mathrm{cm}^{-1}$ and $\sim 10^{-9}\ \Omega^{-1}.\mathrm{cm}^{-1}$,thus in accordance to values previously reported by Banerjee *et.al* [17].

References

[1] P. Mélinon *et al*, "Playing with carbon and silicon at the nanoscale", *Nat. Mater.*, vol. 6, no. 7, pp. 479–490, 2007.

[2] F.Zhu *et al*, "Amorphous Silicon Carbide Photoelectrode for Hydrogen Production from Water using Sunlight", *Sol. Energy*, vol.89, no28-30, pp. 37-41, 2012.

[3] I. A. Digdaya *et al.*, "Extracting large photovoltages from a-SiC photocathodes with an amorphous TiO_2 front surface field layer for solar hydrogen evolution", *Energy and Environmental Science*, vol. 8, no. 5, pp. 1585–1593, 2015.

[4] Y. Catherine *et al*, "Reactive plasma deposited $Si_xC_yH_z$ films," vol. 60, pp. 193–200, 1979.

[5] F. Zhu *et al.*, "Amorphous Silicon Carbide Photoelectrode for Hydrogen Production from Water using Sunlight," *Sol. Energy*,vol. 89, no. 28-30, pp. 37–41, 2012.

[6] J. A. Guerra *et al.*, "The Urbach focus and optical properties of amorphous hydrogenated SiC thin films," *J. Phys. D. Appl. Phys.*, vol. 49, no. 19, 2016.

[7] L. R. Tessler *et al*, "Photoluminescence of tetrahedrally coordinated a-$Si_{1-x}C_x$:H," *Phys. Rev. B*, vol. 52, no. 15, pp. 10962–10971, 1995.

[8] M. H. Kao *et al*, "Low-Temperature Growth of Hydrogenated Amorphous Silicon Carbide Solar Cell by Inductively Coupled Plasma Deposition Toward High Conversion Efficiency in Indoor Lighting," *Sci. Rep.*, vol. 7, no. 1, pp. 1–8, 2017.

[9] R.Vasudevan *et al.*, "A thin-film silicon/silicon hetero-junction hybrid solar cell for photoelectrochemical water-reduction applications," *Sol. Energy Mater. Sol. Cells*, vol. 150, no. March, pp. 82–87, 2016.

[10] K. Takahashi, A. Yoshikawa and A. Sandhu, "*Wide Bandgap Semiconductors Fundamental Properties and Modern*". Springer 2007.

[11] H. Abderrazak *et al.*, "Silicon carbide: Synthesis and properties," *Silicon Carbide Synth. Prop.*, no. C, pp. 361–389, 2008.

[12] J. Bullot *et al.*, "Physics of Amorphous Silicon–Carbon Alloys," *Phys. Status Solidi*, vol. 143, no. 2, pp. 345–418, 1987.

[13] J. A. Luna-López *et al.*, "FTIR, AFM and PL properties of thin SiO_x films deposited by

HFCVD," *Mater. Sci. Eng. B Solid-State Mater. Adv. Technol.*, vol. 174, no. 1–3, pp. 88–92, 2010.

[14] M. Ishimaru *et al.*, "Direct observations of thermally induced structural changes in amorphous silicon carbide," *J. Appl. Phys.*, vol. 104, no. 3, 2008.

[15] J.E.Smith *et al.* "Raman Spectra of Amorphous Si and Related Tetrahedrally Bonded Semiconductors," *Phys. Rev. Lett.*, vol. 26, no. 11, pp. 642–646, 2002.

[16] J. H. Wei and S. C. Lee, "Electrical and optical properties of implanted amorphous silicon," *J. Appl. Phys.*, vol. 76, no. 2, pp. 1033–1040, 1994.

[17] P. K. Banerjee *et al.*, "Electrical and optical properties of aluminum-doped amorphous silicon carbide films," *Appl. surface sci.,* no.983, pp. 288–296, 1991.

[18] T.Kimoto and J.A.Cooper, *"Fundamentals of silicon carbide technology-Growth, characterization, devices and applications", 2014*.

[19] T. Friessnegg *et al.*, "Effect of annealing on the defect structure in *a*-SiC:H films", J. Appl.Phys, vol.80, no.4-15, pp. 2216-2223, 1996.

[20] Y. Vygranenko *et al.*, "Preparation and characterization of a-SiC:H absorber layer for semi-transparent solar cell," *Energy Procedia*, vol. 84, pp. 56–61, 2015.

[21] C. A. Zorman, "Silicon Carbide as a Material for Biomedical Microsystems," *2009 Symp. Des. Test, Integr. Packag. MEMS/MOEMS*, pp. 1–7, 2009.

[22] D. L. Anderson, "Questioning mantle plumes," Amer.Int. Phy., vol. 65, no. 10, pp.10-12 2012.

[23] J.M. Hsu et al., "Characterization of a-SiC:H thin films as an encapsulation material for integrated silicon based neural interface devices,", Thin *solid films,* vol. 516, pp. 34–41, 2007.

[24] L. Han *et al.*, "Gradient dopant profiling and spectral utilization of monolithic thin-film silicon photoelectrochemical tandem devices for solar water splitting," *J. Mater. Chem. A*, vol. 3, no. 8, pp. 4155–4162, 2015.

[25] R.A. Street, "*Hydrogenated amorphous silicon",* Cambridge 1991.

[26] J. Singh and K. Shimakawa, "Advances in amorphous semiconductor," 2003.

[27] P. Y. Yu and M. Cardona, "*Fundamentals of Semiconductors",* Springer 1997.

[28] L.M. Montañez *et al.*, "Optical bandgap enhancement of *a*-SiC through hydrogen incorporation and thermal annealing treatments," *8th Iberoam. Opt. Meet. 11th Lat. Am.*

Meet. Opt. Lasers, Appl., vol. 8785, no. November, p. 8785, 2013.

[29] G. Cherkashinin *et al*., "Mobility edge in hydrogenated amorphous carbon Mobility edge in hydrogenated amorphous carbon," *Appl. Phy.Lett.* , vol. 88, pp. 2004–2007, 2006.

[30] J. Tauc *et al*., "Optical properties and electronic structure of amorphous Ge and Si," *Mat.Res. Bull.*, vol. 3, pp. 37–46, 1968.

[31] *J.A. Guerra et al.*, "Determination of the optical bandgap and disorder energies of thin amorphous SiC and AlN films produced by radio frequency magnetron sputtering," XVII reunion Iberoamericana de Optica y X Encuentros de óptica, láseres y aplicaciones, vol. 274, 2011.

[32] S. K. O'Leary *et al.*, "The relationship between the distribution of electronic states and the optical absorption spectrum of an amorphous semiconductor: An empirical analysis," vol. 82, no.7, pp.3334-3340, 1997.

[33] J. A. Guerra *et al.*, "Band-fluctuations model for the fundamental absorption of crystalline and amorphous semiconductors: a dimensionless joint density of states analysis," *J. Phys. D. Appl. Phys.*, vol. 52, no.10, p.105303, 2018.

[34] L. L. Moseley and T. Luke's, "A simplified derivation of the Kubo-Greenwood formula," *J.Appl. Phy*, vol. 46, pp 476-477, 1978.

[35] J. J. Thevaril *et al.*, "A dimensionless joint density of states formalism for the quantitative characterization of the optical response of hydrogenated amorphous silicon," *J.Appl. Phy*. ,vol.107, pp. 0831051-0831056, 2010.

[36] D. A. Neamen, "*Semiconductor Physics and devices"*, Fourth edition, New York 2002.

[37] Pontus Höjer, "Photoelectrochemical Water- Splitting using 3C-SiC," (Linköping University, Sweden, 2017).

[38] W. Mönch, "Electronic structure of metal-semiconductor", 1st edition 1990.

[39] S.M. Sze and K.N. Kwok, "*Physics of semiconductor devices"*, 3rd edition 2007.

[40] A.A. Ramadam *et al.*, "On the Van der Pauw method of resistivity measurements, "Thin solid film, vol. 239, pp. 272–275, 1994.

[41] L. J. van der Pauw *et al.*, "A method of measuring the resistivity and hall coefficient on lamellae of arbitrary shape," Phillis technical review, vol.20, no. 1, pp. 220–224, 1958.

[42] V.P. Tolstoy, I.V. Chernyshova and V.A. Skryshevsky, *Handbook of Infrared Spectroscopy*. New Jersey 2003.

[43] A. Kamboj, A. K. Saluja and F. Herliscz, *Infrared and Raman characteristic group frequencies*, 3rd edition 2011.

[44] T. Kaneko *et al.*, "FTIR analysis of a-SiC:H films grown by plasma enhanced CVD," *J. Cryst. Growth*, vol. 275, no. 1–2, pp. 1097–1101, 2005.

[45] G. Lucovsky, "Chemical effects on the frequencies of Si-H vibrations in amorphous solids," *Solid state communications*, vol. 29, pp. 571–576, 1979.

[46] H. Kuzmany, "Infrared and Raman spectroscopy: Methods and applications," New York 1995.

[47] H.J. Lin *et al.*, "Effect of the hydrogen concentration on the growth mechanism of sputtered hydrogenated silicon thin films," *Opt. Mater. Expr.*, vol. 3, no.9, p.1215, 2013.

[48] Swanepoel *et al.*, "Determination of the thickness and optical constants of amorphous silicon," *J. Phys. E.*, vol. 16, no. 27, 1983.

[49] C. Yuen *et al.*, "Improving surface-enhanced Raman scattering effect using gold-coated hierarchical polystyrene bead substrates modified with postgrowth microwave treatment," *J. Biomed. Opt.*, vol. 13, no. 6, p. 064040, 2008.

[50] B. Goldstein *et al.*, "Properties of p+ microcrystalline films of SiC:H deposited by conventional rf glow discharge," *Appl. Phys. Lett.*, vol. 53, no. 26, pp. 2672–2674, 1988.

[51] D.A. Skoog and D.M. West, *Principles of instrumental analysis*, 2nd edition 1980.

[52] S. B. K. Moorthy, *Thin film structures in energy applications*. Springer 2015.

[53] G. L. Glish *et al.*, "The basics of mass spectrometry in the twenty-first century," *Nat. Rev. Drug Discov.*, vol. 2, no. 2, pp. 140–150, 2003.

[54] Y. Singh *et al.*, "Electrical Resistivity Measurements: A Review," *Int. J. Mod. Phys. Conf. Ser.*, vol. 22, pp. 745–756, 2013.

[55] C. Ye *et al.*, "Influence of rapid thermal annealing temperature on structure and electrical properties of high permittivity HfTiO thin film used in MOSFET," *Microelectron. Reliab.*, vol. 54, no. 2, pp. 388–392, 2014.

[56] S. Gallis *et al.*, "Comparative study of the effects of thermal treatment on the optical properties of hydrogenated amorphous silicon-oxycarbide," *J. Appl. Phys.*, vol. 102, no. 2, 2007.

[57] M. Hartel *et al.*, "Amorphous Si_xC_{1-x}:H single layers before and after thermal annealing: Correlating optical and structural properties," *Sol. Energy Mater. Sol. Cells*, vol. 94, no.

11, pp. 1942–1946, 2010.

[58] V. E. Vamvakas, "Comparison of FTIR Transmission Spectra of Thermally and LPCVD SiO [sub 2] Films Grown by TEOS Pyrolysis," *Journal Electrochemical Soc.*, vol. 151, no. 5, p. F93, 2004.

[59] A. L. Baia Neto *et al.*, "Annealing effects on near stoichiometric a-SiC:H films," vol. 121, pp. 395–400, 1999.

[60] A. Jean *et al.*, "Characterization of a-SiC:H films produced in a standard plasma enhanced chemical vapor deposition system for x-ray mask application," *J. Appl. Phys.*, vol. 72, no. 7, pp. 3110–3115, 2002.

[61] T. Y. Lin *et al.*, "Fabrication of low-stress plasma enhanced chemical vapor deposition silicon carbide films," *Japanese J. Appl. Physics*, vol. 39, no. 12 A, pp. 6663–6671, 2000.

[62] Y. Katayama, K. Usami, and T. Shimada, "Chemical bonding states in the amorphous spectroscopy and infrared absorption spectra," *Philosophy Magazine,* vol. 43, no.2 ,2015.

[63] S. Gallis *et al.*, "Silicon oxycarbide thin film and nanostructures: synthesis, properties and applications" *Intech open*, vol. 2, pp. 277-302, 2015.

[64] A.V. Vasin *et al.*, "Comparative study of annealing and oxidation effects in a-SiC:H and a-SiC thin films deposited by radio-frequency magnetron sputtering," *Thin Solid Films*, vol. 519, no. 7, pp. 2218–2224, 2011.

[65] G. DellaMea *et al.*, "Influence of hydrogen on the evolution of structural properties of amorphous silicon carbide," *J. Non. Cryst. Solids*, vol. 137–138, pp. 95–98, 1991.

[66] A. Lorinczi *et al.*, "Substrate influence on the X-ray diffraction patterns of amorphous chalcogenide thin films deposited on silicon wafers," *Thin solid films*, vol. 408, pp. 282–285, 2002.

[67] D. Song *et al.*, "Structural characterization of annealed Si_{1-x} Cx / SiC multilayers targeting formation of Si nanocrystals in a SiC matrix,", vol.103, pp. 1–7, 2008.

[68] R.D. White *et al.*, "The stability of halloysite nanotubes in acidic and alkaline aqueous suspensions," vol. 23, 2012.

[69] T. Deschaines *et al.*, "Characterization of Amorphous and Microcrystalline Silicon using Raman Spectroscopy," *Thermo Fisher Appl. Note 51735*, p. 3, 2009.

[70] G. Compagni *et al.*, "Vibrational analysis of compositional disorder in amorphous silicon carbon alloys," *Europhysics Letter"*, vol. 41, no. 2, pp. 225–230, 1998.

[71] M. A. Ouadfel *et al.*, “Applied Surface Science Si-rich a-$Si_{1-x}C_x$ thin films by d.c. magnetron co-sputtering of silicon and silicon carbide: Structural and optical properties,” *Appl. Surf. Sci.*, vol. 265, pp. 94–100, 2013.

[72] R. K. Tripathi *et al.*, “RSC Advances Investigations on phosphorous doped hydrogenated amorphous silicon carbide thin films deposited by a filtered cathodic vacuum arc technique for photo detecting applications,” *RSC Adv.*, vol. 4, pp. 54388–54397, 2014.

[73] W. Yu *et al.*, “Structural and optical properties of hydrogenated amorphous silicon carbide films by helicon wave plasma-enhanced,” *J.Appl.Phys.*, vol.37, pp.3304-3308, 2004.

[74] H. Colder *et al.*, “Characterization of SiC Thin Film Obtained by Magnetron Reactive Sputtering: IBA, IR and Raman Studies.,” *Mat.Sci. For.*, vol. 485, pp. 287–290, 2005.

[75] S. Yang *et al.*, “Hydrogenated amorphous silicon carbide thin films deposited by plasma-enhanced chemical vapor deposition,” no. ICSEEE, pp. 755–758, 2015.

[76] M. Ishimaru *et al.*, “Structural Relaxation of Amorphous Silicon Carbide,” *Phy.Rev.*, vol.89, no.5, pp. 3–6, 2002.

[77] F. Zhang *et al.*, “Effect of high-temperature annealing on the optical-absorption edge of hydrogenated amorphous silicon-carbon films,” *Phy.Rev.*, vol. 46, no. 8, pp. 4590–4594, 1992.

[78] H. C. Card *et al.*, “Aluminum-Silicon Schottky Barriers and Ohmic Contacts in Integrated Circuits,” *IEEE Trans. Electron Devices*, vol. 23, no. 6, pp. 538–544, 1976.

[79] N. Khelifati *et al.* “Effects of Hydrogen Partial Pressure on Boron-Doped Hydrogenated Amorphous Silicon (a-Si:H(B)) Properties,” *Mater. Sci. Forum*, vol. 609, pp. 81–85, 2009.

[80] Dutta *et al.*, “Effect of hydrogenation on the electrical conductivity of amorphous silicon carbide,” *Solid state communication*, vol. 42, no. 3, pp. 219–222, 1982.